Constraints on thermochemical convection of the mantle from plume heat flux, plume excess temperature, and upper mantle temperature

Shijie Zhong[1]

Received 1 August 2005; revised 25 November 2005; accepted 9 January 2006; published 19 April 2006.

[1] Seismic and geochemical observations indicate a compositionally heterogeneous mantle in the lower mantle, suggesting a layered mantle. The volume and composition of each layer, however, remain poorly constrained. This study seeks to constrain the layered mantle model from observed plume excess temperature, plume heat flux, and upper mantle temperature. Three-dimensional spherical models of whole mantle and layered mantle convection are computed for different Rayleigh number, internal heat generation, buoyancy number, and bottom layer thickness for layered mantle models. The model results show that these observations are controlled by internal heating rate in the layer overlying the thermal boundary layer from which mantle plumes are originated. To reproduce the observations, internal heating rate needs $\sim$65% for whole mantle convection, but for layered mantle models, the internal heating rate for the top layer is $\sim$60–65% for averaged bottom layer thicknesses $<\sim$1100 km. The heat flux at the core-mantle boundary (CMB) is constrained to be $\sim$12.6 TW for whole mantle convection. For layered mantle, an upper bound on the CMB heat flux is $\sim$14.4 TW. For mantle secular cooling rate of $\sim$80 K/Ga, the current study suggests that the top layer of a layered mantle is relatively thick (>2520 km) and has radiogenic heat generation rate $>2.82 \times 10^{-12}$ W/kg that is >3 times of that for the depleted mantle source for mid-ocean ridge basalts (DMM). For the top layer to have the radiogenic heat generation of the DMM, mantle secular cooling rate needs to exceed 145 K/Ga. The current study also shows that plume temperature in the upper mantle is about half of the CMB temperature for whole mantle convection or $\sim$0.6 of temperature at compositional boundary for a layered mantle, independent of internal heating rate and Rayleigh number. Finally, the model calculations confirm that mantle plumes accounts for the majority ($\sim$80%) of CMB heat flux in whole mantle convection models. However, plume heat flux decreases significantly by as much as a factor of 3, as plumes ascend through the mantle to the upper mantle, owing to the adiabatic and possibly diffusive cooling of the plumes and owing to slight ($\sim$180 K) subadiabaticity in mantle geotherm.

Citation: Zhong, S. (2006), Constraints on thermochemical convection of the mantle from plume heat flux, plume excess temperature, and upper mantle temperature, *J. Geophys. Res.*, *111*, B04409, doi:10.1029/2005JB003972.

1. Introduction

[2] Recent seismic studies including tomographic imaging [*Su and Dziewonski*, 1997; *Masters et al.*, 2000; *Ishii and Tromp*, 1999] and waveform modeling [*Ni et al.*, 2002, 2005; *Wen et al.*, 2001; *Wang and Wen*, 2004] indicate that the mantle is compositionally heterogeneous, particularly at large depths in the lower mantle below the Pacific and Africa. A compositionally heterogeneous mantle appears to be broadly consistent with geochemical observations that suggest the existence of mantle reservoirs of different compositions from which different volcanic rocks are derived [e.g., *Hofmann*, 1997]. For example, mid-ocean ridge basalts (MORB) are thought to be derived from a shallow or top layer that is more depleted in incompatible elements including radioactive elements, while oceanic island basalts (OIB) may originate from a deep or bottom layer that is more enriched with incompatible elements [*Hofmann*, 1997]. However, mantle compositional structure including the volume and composition of each layer remains poorly constrained. In particular, geochemical studies often suggest that the bottom layer is significantly more enriched in radiogenic elements than the top layer and should also account for a significant fraction of the mantle mass [*Hofmann*, 1997; *Workman and Hart*, 2005]. However, many of seismic studies suggest a bottom layer that seems to be too small in volume to be consistent with geochemical requirements [*Su and Dziewonski*, 1997; *Masters et al.*, 2000].

[3] Mantle compositional structure (i.e., isochemical and whole mantle convection versus thermochemical and lay-

[1]Department of Physics, University of Colorado at Boulder, Boulder, Colorado, USA.

0148-0227/06/2005JB003972$09.00

ered mantle convection) has significant effects on the dynamics of the mantle, as demonstrated by studies on heat transfer and mantle structure for a compositionally heterogeneous or layered mantle [*Davaille*, 1999a, 1999b; *Tackley*, 1998, 2002; *Kellogg et al.*, 1999; *Jellinek and Manga*, 2002; *McNamara and Zhong*, 2004, 2005]. Although these studies provide important insights into the dynamics of a layered mantle, little attempt has been made to examine the consequences of a layered mantle to surface observations that may be used to constrain layered mantle models. The main purpose of this study is to examine the effects of a layered mantle on plume dynamics and to constrain layered mantle models by using observations of upper mantle temperature and of mantle plumes including excess temperature and heat flux.

[4] Mantle plumes may be originated from thermal boundary layer (TBL) instabilities at either CMB for a whole mantle model or a compositional interface for a layered mantle, thus carrying important information about the deep mantle. Mantle plumes are important agents to release the heat from the layer underlying the TBL from which the plumes are derived [*Morgan*, 1971; *Davies*, 1988; *Sleep*, 1990]. Although seismic studies have provided strong evidence for mantle plumes [*Wolfe et al.*, 1997; *Montelli et al.*, 2004], some of the most important constraints on plume dynamics come from surface geophysical and geochemical observations that determine in the upper mantle plume excess temperature at 250°–350°C or ~19–27% of the ambient upper mantle temperature of 1280°C [*Schilling*, 1991; *Farnetani*, 1997] and heat flux carried by plumes at ~2.4–3.5 TW or ~6–10% of the total mantle heat flux [*Davies*, 1988; *Sleep*, 1990].

[5] The inferred plume excess temperature, plume heat flux and mantle background temperature have implications for mantle models. In a whole mantle model, the plume heat flux was considered as heat flux from the core to the mantle [*Davies*, 1988; *Sleep*, 1990], and the plume heat flux was used to estimate the internal heating rate for the mantle convection at 90% and to study the evolution of the core and mantle [*Davies*, 1999]. For a layered mantle, the plume heat flux should reflect the heat flux from the bottom to top layers of the mantle, thus posing constraints on the layered mantle model. For example, it was suggested that the classical layered mantle model with layering at the upper and lower mantle boundary was untenable [*Davies*, 1999], because it would result in too large plume heat flux than the observed with the lower mantle being significantly more enriched with heat-producing elements [*Hofmann*, 1997]. It was suggested that plume excess temperature in whole mantle convection models is much larger than the inferred 250°–350°C that however can be reproduced with layered mantle models [*Farnetani*, 1997]. On the other hand, it was suggested that layered mantle models may lead to upper mantle temperature that is too small compared with the observed [*Spohn and Schubert*, 1982; *McNamara and van Keken*, 2000].

[6] However, a number of important questions need to be resolved for these observations to be useful in constraining mantle models. First, it has been pointed out that in a whole mantle convection model, the estimated plume heat flux may only represent a lower bound on the CMB heat flux, because part of the CMB heat flux should be consumed to heat up downwelling slabs that reach the CMB [*Labrosse*, 2002]. Therefore the estimated plume heat flux at the upper mantle depths may only represent a fraction of heat flux either from the core in a whole mantle convection model or from the bottom layer of a layered mantle. Second, the effects of layered mantle on plume excess temperature [*Farnetani*, 1997] and upper mantle temperature [*Spohn and Schubert*, 1982; *McNamara and van Keken*, 2000] were examined in either transient models with a single plume or parameterized convection models. It is necessary to examine steady state solutions in fully dynamic models.

[7] In this study, using both isochemical and thermochemical convection models in 3-D spherical geometry with extended-Boussinesq approximation we examine the controls on these three observables: plume heat flux, plume excess temperature and the upper mantle temperature. We investigate to what extent plume heat flux represents the heat loss of the layer underlying the TBL from which plumes are originated and what constraints these observations may collectively pose on the mantle models. Different from previous studies that mostly focused on only one of these three observables using 2-D models with a single plume or parameterized convection models, the current study examines simultaneously all these three observables in 3-D spherical models with fully dynamic plumes. In what follows, we will first describe 3-D models of mantle plumes and methods to quantify plume observations. We will then present results for isochemical and thermochemical models. Before presenting conclusions, we will discuss the implications of our results for layered mantle models, geochemistry and heat budget of the Earth.

2. Models and Methods

[8] We consider isochemical (whole mantle convection) and thermochemical (layered mantle) models with extended-Boussinesq approximation in 3-D regional spherical geometry for incompressible fluids with depth- and temperature-dependent viscosity, and depth-dependent thermal conductivity and coefficient of thermal expansion. The basic physical processes of thermal convection can be described by the conservation laws of mass, momentum, and energy. The nondimensional governing equations are

$$\nabla \cdot \boldsymbol{u} = 0, \tag{1}$$

$$-\nabla P + \nabla \cdot \left[\eta\left(\nabla \boldsymbol{u} + \nabla^T \boldsymbol{u}\right)\right] + \xi\left[\alpha Ra(T - \beta C) + \sum_k \left(Ra_k \Gamma_k\right)\right]\boldsymbol{e_r} = 0, \tag{2}$$

$$\left[1 + \sum_k \omega_k^2 \frac{Ra_k}{Ra}\frac{d\Gamma_k}{d\pi_k} D_i (T + T_s)\right]\left(\frac{\partial T}{\partial t} + \boldsymbol{u} \cdot \nabla T\right) + \left(\alpha + \sum_k \omega_k \frac{Ra_k}{Ra}\frac{d\Gamma_k}{d\pi_k}\right)(T + T_s) D_i u_r = \nabla \cdot (\kappa \nabla T) + \frac{D_i}{\xi Ra}\sigma_{ij}\frac{\partial u_i}{\partial x_j} + H, \tag{3}$$

$$\frac{\partial C}{\partial t} + \boldsymbol{u} \cdot \nabla C = 0, \tag{4}$$

Table 1. Physical Parameters and Constants

Parameters	Value
Earth radius R_e	6370 km
Mantle thickness D	2866.5 km
Surface thermal expansivity α_0[a]	5×10^{-5}/K
Surface thermal diffusivity κ_0[a]	10^{-6} m^2/s
Surface density ρ_0	3300 kg/m^3
Specific heat C_p	1200 J/(kg·K)
Gravitational acceleration g	9.8 m/s^2
Surface temperature T_s'	273 K
Olivine-spinel phase change	
Clayperon slope γ_1	3 MPa/K
Density change $\Delta\rho_1/\rho_0$	7.8%
Spinel-Pervoskite phase change	
Clayperon slope γ_2	−3 MPa/K
Density change $\Delta\rho_2/\rho_0$	7.8%

[a]Thermal expansivity decreases by a factor of 5 from surface to the CMB, while thermal conductivity increases by a factor of 2.18 from surface to the CMB.

where $\boldsymbol{u}$, P, η, α, T, κ, T_s, D_i, u_r, σ_{ij} and H are the velocity vector, pressure, viscosity, coefficient of thermal expansion, temperature, thermal diffusivity, surface temperature, dissipation number, radial velocity, deviatoric stress, and heat production rate, respectively; $\xi = (R_e/D)^3$ with R_e as the Earth's radius and D as the mantle thickness; C represents the composition and is only relevant for thermochemical convection models, and C is 0 and 1 for mantle materials in the top and the bottom layers of a layered mantle, respectively; Γ_k, ω_k, and π_k are phase function, Clapeyron slope, and excess pressure for phase k (k = 1 and 2 for olivine-spinel and spinel-pervoskite phase changes, respectively), respectively [*Christensen and Yuen*, 1985]; $\boldsymbol{e_r}$ is the unit vector in radial direction; and Ra, β, and Ra_k are a Rayleigh number, compositional buoyancy number, and phase change Rayleigh number for phase change k, respectively. These equations were obtained by using the following characteristic scales: length R_e, time R_e^2/κ_0, and temperature ΔT. Ra, β, Ra_k, D_i, and H are defined as

$$Ra = \alpha_0\rho_0 g\Delta T D^3/(\kappa_0\eta_0), \tag{5}$$

$$\beta = \Delta\rho/(\alpha\rho_0\Delta T), \tag{6}$$

$$Ra_k = \Delta\rho_k g D^3/(\kappa_0\eta_0), \tag{7}$$

$$D_i = \alpha_0 g R_e/C_p, \tag{8}$$

$$H = \gamma R_e^2/\left(C_p\kappa_0\Delta T\right), \tag{9}$$

where α_0, and κ_0, and ρ_0 are the reference coefficient of thermal expansion, thermal diffusivity, and mantle density that are all taken as the values at the surface, η_0 is the reference viscosity that is taken as the viscosity at the bottom boundary, $\Delta T = T_b' - T_s'$ is the temperature difference across the mantle with T_b' and T_s' as the CMB and surface temperature, respectively (T_s' = 273 K), $\Delta\rho$ is density difference between the two compositions; $\Delta\rho_k$ is the density change for phase change k, C_p is the specific heat, g is the gravitational acceleration, and γ is internal heat generation rate. Notice that in the definition of buoyancy number β, α is the coefficient of thermal expansion at the density interface. All the relevant parameters are given in Table 1. It should be pointed out that for isochemical models with $\beta = 0$, equations (1)–(3) become identical to those given by *Christensen and Yuen* [1985].

[9] The models are formulated in a regional spherical geometry, and the computational domain is from 40° to 140° in colatitude, 0° to 110° in longitude, and r_i = 0.55 to r_o = 1 in radius (Figure 1). The surface and CMB are isothermal and free-slip, while along the side boundaries thermally insulating and free-slip boundary conditions are used. From the surface to CMB, thermal conductivity increases by a factor of 2.18 and the coefficient of thermal expansion α decreases by a factor of 5 [e.g., *Tackley*, 2002]. Mantle viscosity is both depth and temperature dependent, and nondimensional viscosity is given by

$$\eta = \left(1 - 0.9\frac{r - r_i}{r_o - r_i}\right)\eta_r \exp\left\{E\left[1 - \frac{(T - T_{adi}(r) + T_{adi}(r_{ttbl}))}{\Delta T_{s\_a}}\right]\right\}, \tag{10}$$

where η_r is 1/30 between 100 km and 670 km depths and is 1 otherwise, E is the nondimensional activation energy, ΔT_{s_a} is the total super-adiabatic temperature difference from the CMB to surface, and $T_{adi}(r)$ is the adiabatic temperature at radius r and is determined by downward integration of adiabatic gradient $g\alpha(r)T_{ave}(r)/c_p$ [*Turcotte and Schubert*, 2002] from the base of the top thermal boundary layer r_{ttbl} where the adiabatic temperature is $T_{adi}(r_{ttbl})$ and $T_{ave}(r)$ is the averaged temperature. E is 6.90776 for this study and it gives rise to 10^3 viscosity variations (i.e., mobile-lid convection) for super-adiabatic temperatures varying from the surface to CMB. In addition to the temperature-dependent viscosity, the radial viscosity includes a factor of 30 reduction between 100 km and 670 km depths and an additional factor of 10 linear increase from the surface to the CMB, and this is broadly consistent with that from long-wavelength geoid studies [*Hager and Richards*, 1989].

[10] Given the large number of parameters involved in the models, we need to identify controlling parameters that we may vary systematically, while fixing other parameters. Table 1 lists all the fixed parameters including those for the phase changes, thermal diffusivity and coefficient of thermal expansion. For isochemical models, two controlling parameters are Rayleigh number Ra and internal heat generation rate H, while for thermochemical models, two additional controlling parameters are buoyancy number β and average thickness for the bottom layer d_b. Notice that reference viscosity η_0 and temperature difference across the mantle ΔT are not specified and they are related to each other through Ra (equation (5)).

[11] The governing equations are solved with a finite element code CitcomCU. CitcomCU was derived from an original Cartesian code Citcom [*Moresi and Gurnis*, 1996] but with many new extensions. CitcomCU works in both 3-D Cartesian and regional spherical geometries for isochemical and thermochemical convection with either

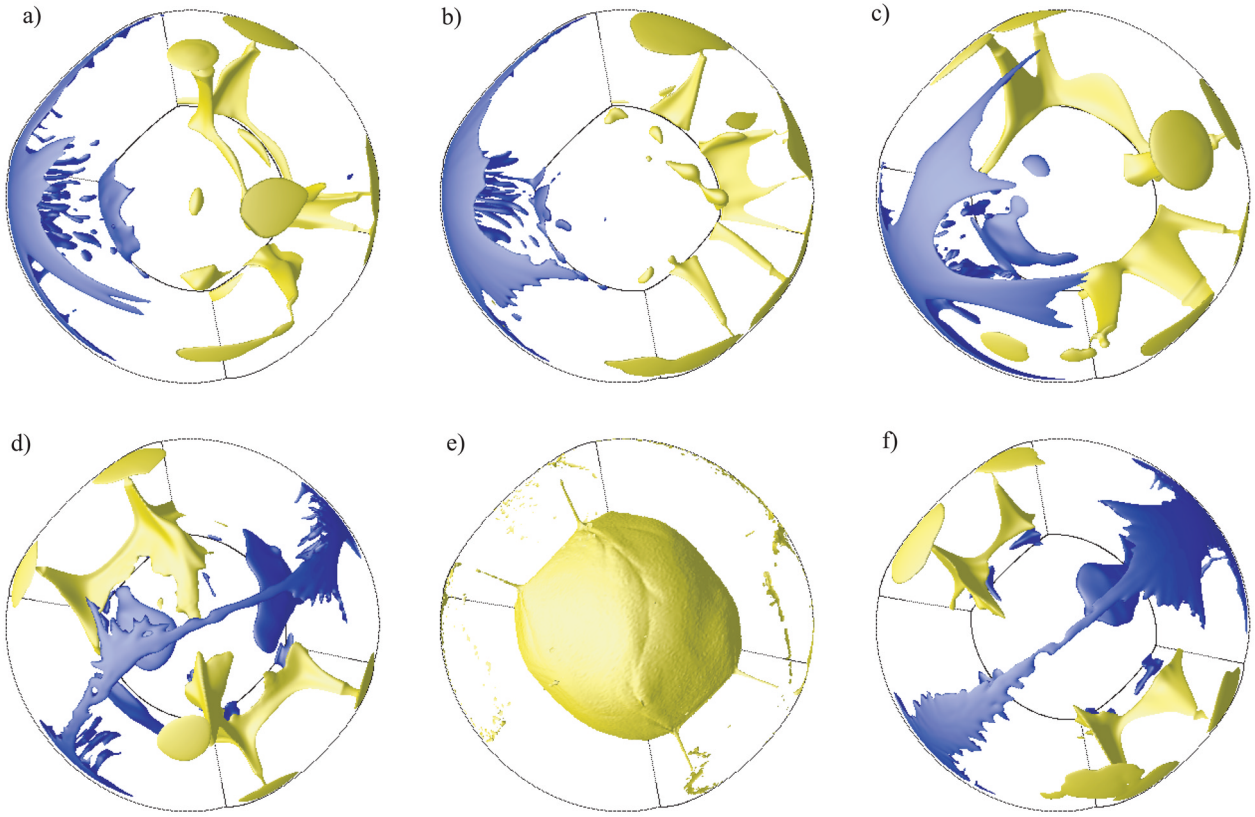

Figure 1. Snapshots of residual temperature fields for Cases (a) WM1, (b) WM3, (c) WM2, (d) LMA1, and (f) LMA3, and (e) snapshot of composition field for Case LMA1. Figures 1d and 1e are for the same time step for Case LMA1. The yellow and blue isosurfaces for residual temperature are for 0.1 and −0.1, respectively.

Boussinesq or extended-Boussinesq approximation. The numerical methods and benchmark cases for both isochemical and thermochemical convection models are presented in Appendix A.

[12] All the model calculations except for resolution tests are done with 256 × 192 × 64 (colatitudinal, longitudinal, and radial directions, respectively) elements and ∼5 × 10^7 particles (applicable only for thermochemical cases). Numerical grids are refined near the TBLs and in the upper mantle. In this study, we are only interested in statistically steady state results. For an isochemical model, we often take a temperature field from a similar model as initial field and integrate the model for on average ∼70,000 time steps to an approximately statistically steady state. For a thermochemical model, we first compute a 2-D spherically axisymmetric geometry model with identical thermochemical convection parameters to a steady state using a finite element code [*Roberts and Zhong*, 2004], and the resulting horizontally averaged temperature superimposed with random perturbation is then used as initial temperature for the 3-D calculation which often takes ∼25,000 time steps to a steady state. After each model (isochemical and thermochemical) reaches a statistically steady state, the model is integrated for another 20,000 time steps or 5–10 transit times. Only the steady state results of heat flux, plume heat flux, plume excess temperature, upper mantle temperature, and other model outputs are quantified and analyzed. Each model run on average takes ∼8 days on 24 Pentium 4 Xeon 2.4 GHz Processors.

3. Results

3.1. Isochemical Models

[13] In total, 21 isochemical and thermochemical models with different controlling parameters are computed. We first present eight isochemical models in which internal heat generation H varies between 18 and 108 and Rayleigh number Ra varies from 1.33 × 10^7 to 1.2 × 10^8 (Table 2). For Case WM1 with $Ra = 1.2 \times 10^8$ and $H = 72$, a snapshot of representative thermal structure in a statistically steady state shows downwellings and upwelling plumes, and the convection is time dependent (Figures 1a and 2a). The downwellings indicate that the convection is in a mobile lid regime, characteristic of Earth's plate tectonic style of mantle convection. Plumes thin as they ascend and are significantly thinner in the upper mantle, owing to the depth-dependent viscosity that also results in larger flow velocity in the upper mantle (nondimensional velocity of ∼10^4 or 5 cm/yr) than that in the lower mantle (Figure 2b). By time-averaging surface and CMB heat fluxes Q_s and Q_{cmb} (Figure 2a), we find that internal heating rate $\zeta_m = (Q_s - Q_{cmb})/Q_s$ is 51%. Latent heating of the phase changes results in elevated temperature in the transition zone and adiabatic heating leads to adiabatic temperature gradient (Figure 2c for $T_{ave}(r)$ that is

Table 2. Models Parameters and Results

Case	Ra (10^7)	H[a]	β	d_b, km	$\zeta_m(\zeta_{stop})$, %	Q_{plume_um},[b] %	T_{um}	$T_p(r_{um})$[b]	ΔT_{plume_um},[b] %	Q_s[c]	V_s (10^3)[c]
WM1	12	72			51	12.4(4)	0.358	0.496(0.050)	38(14)	29.9	8.20
WM1r[d]	12	72			51	14.1(5)	0.359	0.489(0.043)	37(12)	29.7	8.02
WM2	12	36			34	26.5(10)	0.297	0.513(0.055)	73(19)	26.4	6.92
WM3	12	108			65	7.3(3)	0.404	0.517(0.038)	28(10)	36.0	10.9
WM4	4	18			24	29.4(9)	0.289	0.481(0.049)	67(17)	18.6	3.19
WM5	4	36			43	20.2(7)	0.330	0.491(0.053)	49(16)	21.6	4.61
WM6	4	72			61	9.5(3)	0.389	0.518(0.037)	33(10)	25.6	5.34
WM7	4	108			74	5.1(1)	0.443	0.525(0.019)	18(4)	30.1	6.20
WM8	1.33	36			51	14.1(3)	0.364	0.509(0.035)	40(10)	17.6	2.49
LMA1	12	36(108)	1	637	65(43)	17.5(2)	0.261	0.367(0.019)	41(7)	17.7	2.53
LMA2	12	54(108)	1	637	76(56)	12.2(2)	0.300	0.388(0.027)	29(9)	21.2	3.50
LMA3	12	72(108)	1	637	78(61)	10.2(2)	0.325	0.407(0.020)	25(6)	23.2	3.51
LMA3r[d]	12	72(108)	1	637	78(60)	10.7(2)	0.325	0.402(0.017)	24(5)	23.0	3.45
LMA4	12	36(54)	1	637	54(41)	16.6(1)	0.257	0.352(0.025)	37(10)	16.9	2.56
LMA5	4	18(108)	1	637	63(31)	19.1(2)	0.246	0.344(0.032)	41(13)	12.1	1.25
LMA6	4	36(108)	1	637	78(52)	14.3(1)	0.295	0.385(0.022)	31(8)	15.5	1.63
LMA7	4	72(108)	1	637	90(70)	10.6(1)	0.372	0.450(0.006)	21(2)	21.5	2.24
LMA8	4	72(108)	3/2	637	89(70)	11.1(2)	0.368	0.449(0.006)	22(2)	21.9	2.25
LMA9	4	72(108)	2/3	637	89(70)	9.9(2)	0.368	0.447(0.011)	21(3)	22.5	2.01
LMB1	12	18(108)	1	1121	54(10)	30.3(1)	0.227	0.343(0.028)	51(12)	15.2	1.44
LMB2	12	36(108)	1	1121	63(26)	22.8(1)	0.263	0.373(0.020)	42(8)	17.4	1.53
LMB3	12	72(108)	1	1121	85(55)	10.3(1)	0.327	0.414(0.030)	26(9)	24.0	3.84
LMB4	12	108(108)	1	1121	92(65)	5.4(1)	0.375	0.435(0.020)	16(5)	28.1	4.30

[a]The numbers in and out of parentheses are the heat generation for the bottom and top layers, respectively.
[b]The numbers in parentheses are the standard deviations.
[c]Q_s and V_s are the averaged surface heat flux and velocity, respectively. The scalings for heat flux and velocity are $k_0\Delta T/R_e$ and $\kappa_0 R_e$, respectively.
[d]These cases are for resolution tests.

averaged both horizontally and in time). Adiabatic temperature is also determined by integrating adiabatic gradient $g\alpha(r)T_{ave}(r)/c_p$ [*Turcotte and Schubert*, 2002] from the base of the top TBL to the CMB (Figure 2c). Comparison of the adiabatic temperature with $T_{ave}(r)$ shows sub-adiabatic temperature with its maximum of ~0.053 immediately above the bottom TBL, which correspond to ~180 K for $\Delta T = 3400$ K.

[14] A key aspect of this study is to quantify the three observables in numerical models: the background mantle temperature, plume heat flux, and plume excess temperature. At a given time step, we compute horizontally averaged temperature $T_{bg}(r)$ excluding cold downwellings (i.e., only considering where $T \geq T_{ave}(r)$). The upper mantle temperature is $T_{bg}(r_{um})$ at radius $r_{um} = 0.9529$ (i.e., $r = 6070$ km or depth of 300 km). Applying time average to $T_{bg}(r_{um})$ gives the first observable, the upper mantle temperature T_{um}. It should be pointed out that $T_{bg}(r)$ differs only slightly from $T_{ave}(r)$ and the differences are ~1% in the upper mantle and ~2% at large depths in the lower mantle. However, because the inferences of the upper mantle temperature, plume excess temperature and plume heat flux are all made with respect to the normal upper mantle outside subduction zones, we think that it is more appropriate to use $T_{bg}(r)$.

[15] To quantify plume-related observables, we first define and locate upwelling plumes. The following scheme is used. (1) For a given time step and radius r, search through the temperature field to find the maximum temperature T_{max}. (2) Search through the temperature field to find a maximum temperature T_i and its location (θ_i, ϕ_i) and take T_i as plume temperature for plume i. Continue to step 3 if $T_i > T_{bg}(r) + f[T_{max} - T_{bg}(r)]$ for a given threshold parameter f. Otherwise, go back to step 1 for next radius. (3) For plume i, search the elements within arc distance of r_{arc} from its center location (θ_i, ϕ_i) to determine its plume region. An element belongs to plume i, if its radial velocity u_r is positive (i.e., upward) and its temperature $\geq T_{bg}(r)$. (4) Exclude the plume region for plume i for consideration for next plume and go back to step 2 to search for next plume. At the end of the process, the number of plumes and temperature for each plume at each radius are determined. While parameter f determines threshold temperature at plume centers, r_{arc} controls the maximum radial extend of a plume. In this study, f and r_{arc} are set to be 0.2 and 0.15 (i.e., 950 km), respectively. Temperature fields and plume regions identified by the above scheme are shown in Figure 3 for two different depths for thermal structure in Figure 1a. Notice that plumes in Figure 3d identified from our detection scheme tend to occupy larger regions than those in Figure 1a. This is because $T \geq T_{bg}(r)$ criterion is used in our detection scheme, while Figure 1a is isosurface of certain residual temperature. The effects of the choices of f and r_{arc} on the model results are small and are discussed later. Notice that downwelling regions are also defined in Figures 3c and 3g as where u_r is negative and temperature $\leq T_{ave}(r)$.

[16] To determine plume excess temperature, we take the maximum temperature for each plume T_i at a given depth and then compute the averaged plume temperature $T_p(r)$ at this depth (Figure 2c). Plume excess temperature at 300 km depth normalized by the background temperature ΔT_{plume_um} is then determined by time-averaging $[T_p(r_{um}) - T_{um}]/T_{um}$ at this depth. To quantify plume heat flux, convective heat flux is first defined as $q_{adv} = u_r[T - T_{bg}(r)]$. Conductive heat flux is ignored, and this is justified for convection-dominated regions (i.e., outside the top and bottom TBLs). The q_{adv} is significant and positive for both downwellings and upwellings but is nearly zero in other regions even in some of the plume regions identified by our detection scheme where temperature may be only slightly larger than $T_{bg}(r)$ (Figures 3b and 3f). There are small regions where q_{adv} is slightly negative, and this is caused by upward (downward) advection of relatively

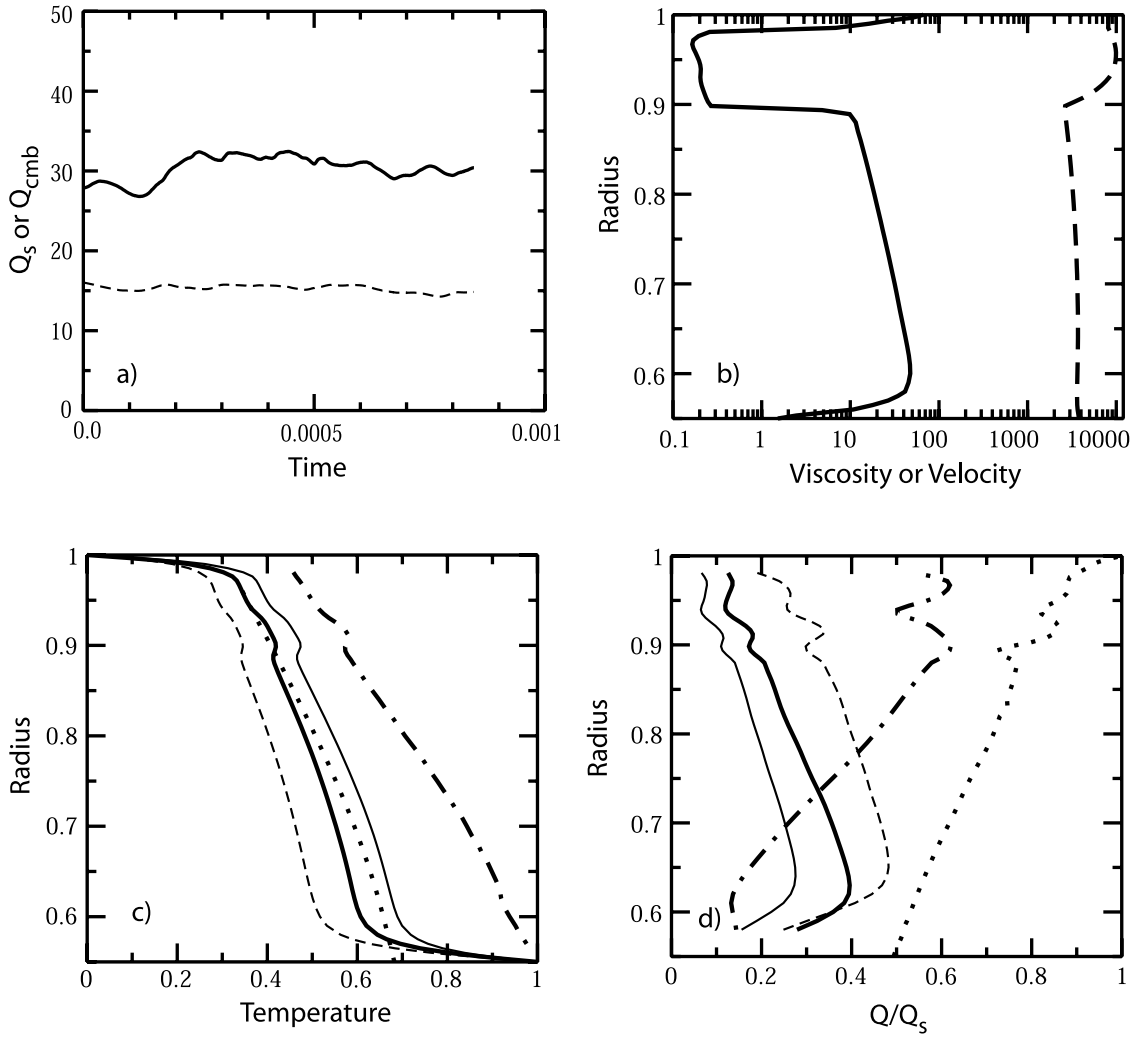

Figure 2. (a) Time-dependent surface (solid line) and CMB (dashed line) heat flux for Case WM1. Only the final stage of the calculations is shown with time = 0 arbitrarily set. (b) Radial dependences of viscosity (solid line) and velocity (dashed line) for Case WM1. (c) Radial dependences of average temperature (thick solid line), plume temperature (dash-dotted line), and adiabatic temperature (dotted line) for Case WM1. Also plotted are average temperatures for Cases WM2 (thin dashed line) and WM3 (thin solid line). (d) Radial dependences of plume heat flux (thick solid line), downwelling heat flux (dash-dotted line), and total heat flux (dotted line) normalized by surface heat flux for Case WM1, and of plume heat flux for Cases WM2 (thin dashed line) and WM3 (thin solid line).

cold (hot) fluids. The total plume heat flux at a given radius r is $Q_p(r) = \int_{S_p} q_{adv} dS$, where S_p is the area for plumes at this radius (Figures 3c and 3g). Plume heat flux at the upper mantle depth, $Q_p(r_{um})$, is the plume heat flux at radius r_{um}, and the normalized upper mantle heat flux by surface heat flux is $Q_{plume\_um} = Q_p(r_{um})/Q_s$. Heat flux associated with downwellings can be defined similarly as $Q_d(r) = \int_{S_d} q_{adv} dS$, where S_d is the area for downwellings at this radius.

[17] The three observables: upper mantle temperature, plume heat flux and plume excess temperature, are computed at 300 km depth and are time-averaged for the steady state results, using the above schemes. For Case WM1, at 300 km depth, mantle temperature T_{um} is 0.358, and plume temperature $T_p(r_{um})$ is 0.496 with standard deviation of 0.050. Plume excess temperature in the upper mantle normalized by the background temperature, T_{um}, ΔT_{plume_um} = 0.38 with standard deviation of 0.14, and upper mantle plume heat flux normalized by Q_s, Q_{plume_um} = 12.4% with standard deviation of 4% (Table 2). These results are not sensitive to the choices of parameters f and r_{arc} that help locate the plumes. For example, reducing f from 0.2 to 0.1 leads to nearly identical results for plume excess temperature ΔT_{plume_um} and plume heat flux Q_{plume_um} with difference at the third significant digit. A resolution test is performed in which the number of elements in horizontal directions is doubled, while the vertical resolution is kept the same due to limitations from the computers (i.e., increasing resolution from 256 × 192 × 64 in Case WM1 to 384 × 256 × 64 in Case WM1r). The test demonstrated the robustness of the results, especially considering the standard deviations (Table 2).

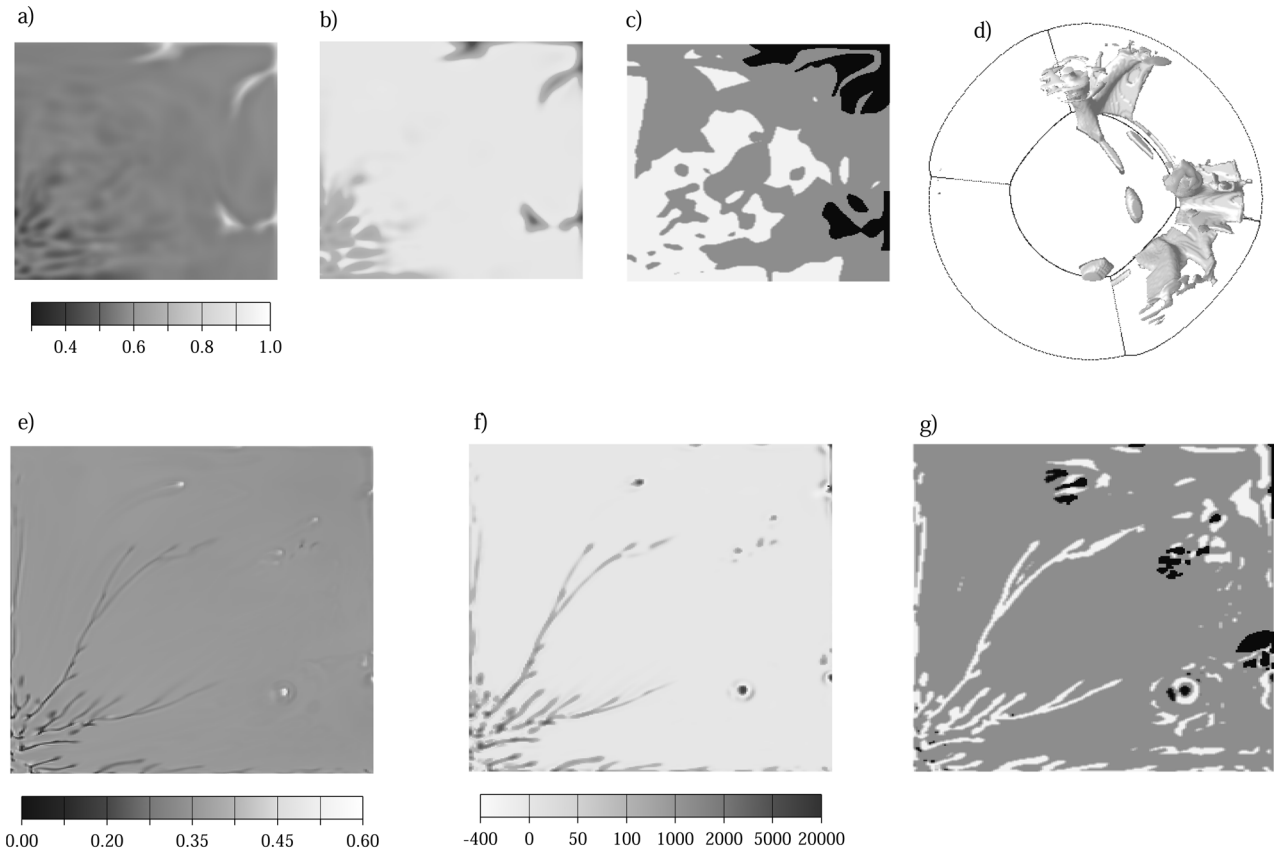

Figure 3. Map views of (a, e) temperature, (b, f) convective heat flux, and (c, g) identified regions of upwelling plumes (black) and downwellings (white) at 1970 km (Figures 3a–3c) and 300 km (Figures 3e–3g) depths, and (d) 3-D representation of identified upwelling plume regions for thermal structure in Figure 1a for Case WM1. In Figure 3d, the top and bottom thermal boundary layers are excluded.

[18] Plume heat flux varies with depth and decreases by a factor of 3.2 from 2360 km (i.e., $r = 0.6295$) to 300 km depths (Figure 2d). Although plume heat flux in the upper mantle Q_{plume_um} accounts for 25.3% of Q_{cmb} (because $Q_{plume\_um} = 12.4\%Q_s$ and $Q_{cmb} = 49\%Q_s$), ~81% of Q_{cmb} is transported by plumes right above the CMB at ~2360 km depth (Figure 2d). The reduced plume heat flux with radius is caused by adiabatic cooling and possibly diffusive cooling of plumes, as indicated by decreasing $T_p(r) - T_{ave}(r)$ with r, and also by the slight subadiabatic temperature (Figure 2c). Notice that in Figure 2d, plume heat flux is only determined outside the top and bottom TBLs, because plume heat flux as convective heat flux is only meaningful outside the TBLs.

[19] Convective heat flux for downwellings Q_d(r) and total heat flux Q(r) (i.e., convective and conductive heat flux) as a function of radial position are also determined (Figure 2d). Q(r) generally increases with radius owing to the internal heating. However, Q(r) also oscillates at 670 km and 410 km depths owing to the latent heating effect. Downwelling heat flux Q_d(r) decreases with depth, and is complementary to plume heat flux Q_p(r). Notice that the sum of Q_d(r) and Q_p(r) may differ slightly from Q(r), because of negative convective heat flux in some regions as discussed earlier.

[20] It is worthwhile to note that for Case WM1 with internal heating rate $\zeta_m = 51\%$, $Q_{plume\_um} = 12.4\%Q_s$ and $\Delta T_{plume\_um} = 0.38$ are significantly larger than the inferred plume heat flux of 6–10% of Q_s and plume excess temperature of 0.19–0.27 of T_{um} (Figures 4a–4c), indicating that the plumes in Case WM1 are too hot and transfer too much heat flux, compared with the observations. However, $T_{um} = 0.358$ is within the observed range of the upper mantle temperature. While mantle temperature of ~1320°C at 300 km depth is relatively well constrained, T_{cmb} has relatively large uncertainties at 3400 ± 500°C [*Boehler et al.*, 1995], which leads to relatively large uncertainty in T_{um} ranging from 0.338 to 0.455. An important goal of this study is to examine the parameter space in which model plumes are consistent with the observed. We hypothesize that it is the internal heating rate ζ_m that controls the plume observables. Seven additional cases with different controlling parameters Ra and H are computed to test this hypothesis.

[21] Cases WM2 and WM3 have internal heat generation rate $H = 36$ and 108, respectively, but are otherwise identical to Case WM1. The larger H is, the larger the mantle temperature (Figure 2c) and internal heating rate ζ_m (Table 2) are. Also, the larger H is, the weaker upwelling plumes are (Figures 1a–1c), which is expected because for entirely internally heated convection, no upwelling plumes are expected. The increase in mantle temperature with H (Figure 2c) causes both plume excess temperature ΔT_{plume_um} and plume heat flux Q_{plume_um} to decrease

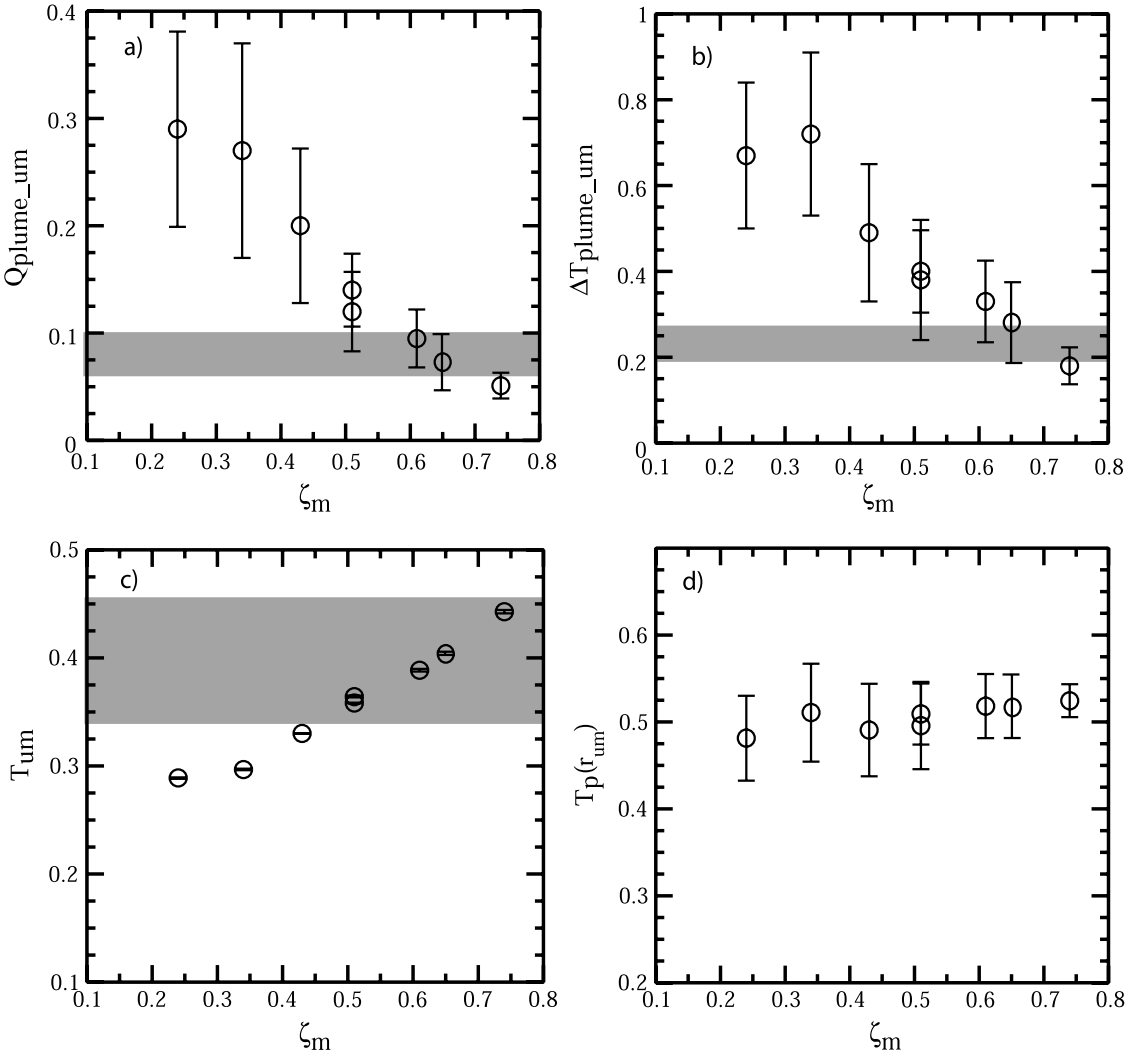

Figure 4. Dependences of (a) plume heat flux Q_{plume_um}, (b) plume excess temperature ΔT_{plume_um}, (c) upper mantle temperature T_{um}, and (d) plume temperature $T_p(r_{um})$ on internal heating rate ζ_m for isochemical models. Standard deviations for Q_{plume_um}, ΔT_{plume_um}, and T_{um} and the range of observed values (shaded horizontal bars) are also plotted in Figures 4a–4c.

(Figure 2d). This is because ΔT_{plume_um} and Q_{plume_um} are both dependent on T_{um} and because plume temperature $T_p(r_{um})$ is insensitive to H (Table 2). For cases WM2 and WM3, ζ_m is 34% and 65%, Q_{plume_um} is 26.5% and 7.3% of Q_s, and ΔT_{plume_um} is 0.73 and 0.28 of T_{um}, and T_{um} is 0.297 and 0.404, respectively (Table 2). Clearly, Case WM3 with larger internal heating rate ζ_m leads to plume heat flux and plume excess temperature that are more consistent with the inferred values for the upper mantle.

[22] Five additional cases (cases WM4–WM8) are computed with Ra varying by a factor of 9 and H varying between 18 and 108 (Table 2). The general trend is that ζ_m decreases with increasing Ra for a fixed H and also decreases with decreasing H for a fixed Ra (Table 2). CMB and surface heat fluxes generally increase with Ra, and for a fixed H this leads to a larger fraction of CMB to surface heat fluxes or smaller internal heating rate ζ_m. For a fixed Ra, surface heat flux decreases with decreasing H, while CMB heat flux is less sensitive to H. This causes ζ_m to decrease with decreasing H for a fixed Ra.

[23] Figures 4a–4c demonstrate the controlling effect of internal heating rate ζ_m on these observables: While the upper mantle temperature T_{um} increases with ζ_m, both plume excess temperature ΔT_{plume_um} and plume heat flux Q_{plume_um} decrease with ζ_m. For isochemical models to satisfy these observations, internal heating rate ζ_m needs to be ~65%. For small ζ_m, plumes are too hot relative to the background mantle temperature and transfer too much heat flux. It is also worthwhile to point out that plume temperature $T_p(r_{um})$ is nearly constant and is ~0.5 for all these cases (Figure 4d), suggesting that $T_p(r_{um})$ be largely controlled by the temperature of the bottom TBL.

[24] These results do not seem to be sensitive to Ra. This may be understood by considering these observables for a simple Cartesian, isoviscous and basal heating thermal convection. It is well known for such a convection, the background temperature is the mean temperature or 0.5, the plume excess temperature is ~0.5, and upwelling plumes and downwellings are each responsible for transferring 50% of the surface heat flux [*Zhong*, 2005], independent of Ra.

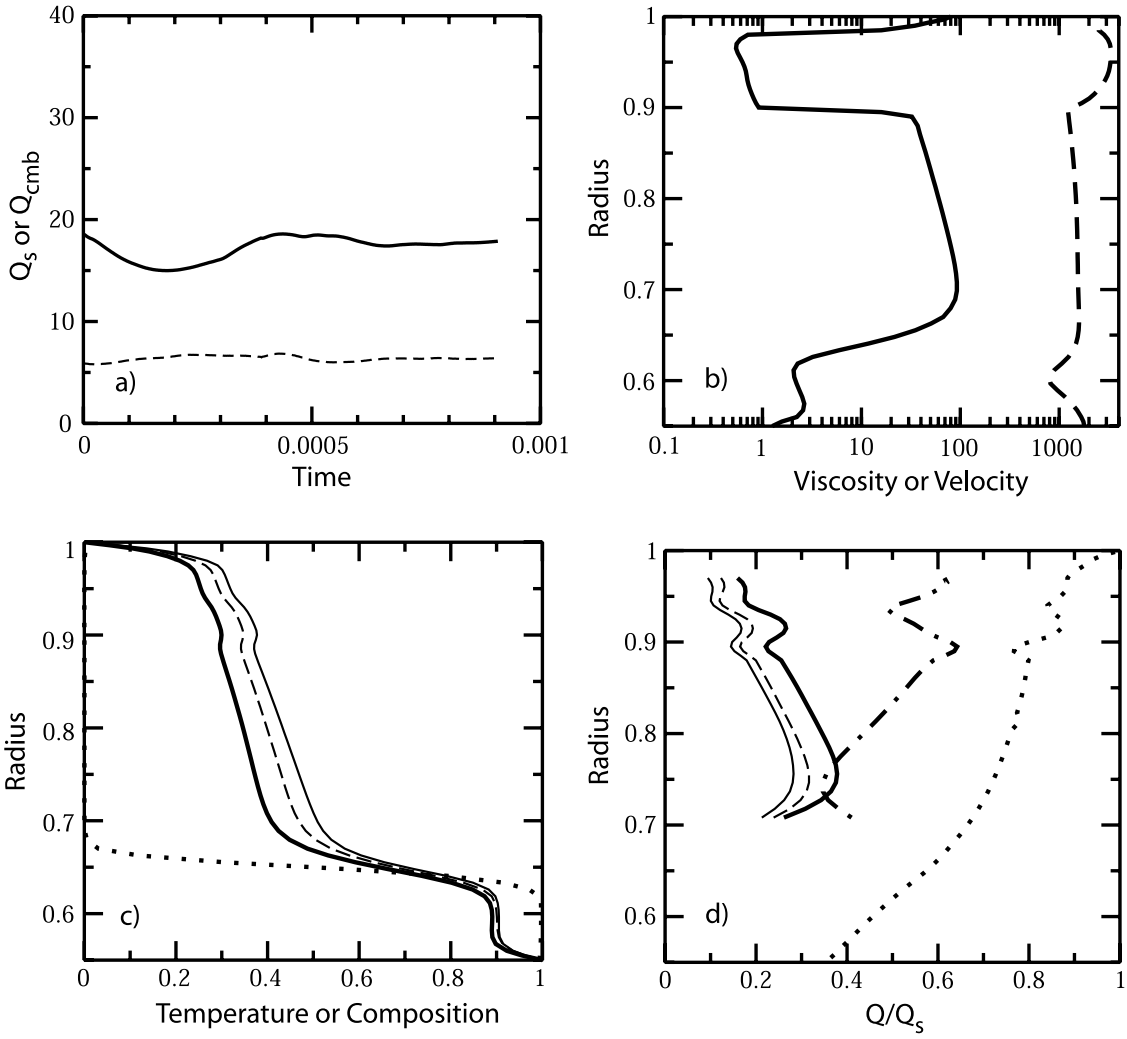

Figure 5. (a) Time-dependent surface (solid line) and CMB (dashed line) heat flux for Case LMA1. Only the final stage of the calculations is shown with time = 0 arbitrarily set. (b) Radial dependences of viscosity (solid line) and velocity (dashed line) for Case LMA1. (c) Radial dependences of average temperature (thick solid line) and composition (dotted line) for Case LMA1 and of average temperature for Cases LMA2 (thin dashed line) and LMA3 (thin solid line). (d) Radial dependences of normalized plume heat flux (thick solid line), downwelling heat flux (dash-dotted line), and total heat flux (dotted line) for Case LMA1, and of plume heat flux for Cases LMA2 (thin dashed line) and LMA3 (thin solid line).

That is, for Cartesian, isoviscous and basal heating convection, T_{um} = 0.5, ΔT_{plume_um} = 1, and Q_{plume_um} = 50%, independent of Ra. For spherical, isoviscous and basal heating convection, considering energy balance at the CMB and surface leads to $T_{um} \sim R_{cmb}^2/(R_e^2 + R_{cmb}^2)$ where R_{cmb} is the core radius, and the resulting upper mantle temperature T_{um} is significantly smaller than that for its Cartesian counterpart, causing plume excess temperature ΔT_{plume_um} and plume heat flux Q_{plume_um} to be significantly larger than their Cartesian counterparts and also larger than the observed values for the upper mantle. Adding internal heating is an effective way to bring these observables to the observed values. The current study shows that for realistic viscosity structure and thermodynamic parameters that are used here, ~65% internal heating rate is needed to explain the observed plume excess temperature, plume heat flux and upper mantle temperature.

3.2. Thermochemical Models

[25] Layered mantle models contain four controlling parameters: buoyancy number β and the bottom layer thickness d_b, in addition to internal heat generation rate H and Rayleigh number Ra. Also, H for the top and bottom layers (H_{top} and H_{botm}) can be different. On the basis of proceeding isochemical models, we hypothesize that the internal heating rate for the top layer ζ_{top} controls those three observables in thermochemical models. In total, 13 thermochemical cases with different controlling parameters are computed to test this hypothesis and to examine the controls on the plume-related observables.

[26] In Case LMA1, $Ra = 1.2 \times 10^8$, d_b = 0.1 (i.e., 637 km), β = 1, H_{top} = 36 and H_{botm} = 108. At a statistically steady state (Figure 5a), Case LMA1 shows upwellings and downwellings in the top layer with upwellings that have two different forms: quasi-cylindrical plumes and linear ridge

structures (Figure 1d). Vigorous convection also exists in the bottom layer but with much smaller temperature anomalies than those for convection in the top layer, as indicated by the RMS of flow velocity that is significant in the bottom layer, but less than that in the top layer (Figure 5b), and by the horizontally averaged temperature $T_{ave}(r)$ that displays an additional TBL at the compositional boundary (Figure 5c).

[27] The compositional boundary is deformed by downwellings and upwelling (Figures 1d and 1e). While the upwelling plumes entrain dense materials from the bottom to top layers, the bottom layer entrains the light materials from the top layer as sheet-like structure below the linear ridge upwelling structures, suggesting a mechanical coupling between the two layers. Entrainment with similar plume and sheet structures in the top and bottom layers was reported in laboratory models in which the top layer is less viscous and less dense than the bottom layer [*Davaille*, 1999b]. However, owing to the temperature dependent viscosity, the top layer in the current study is significantly (a factor of ~20) more viscous than the bottom layer (Figure 5b). The entrainment should eventually mix the two components and destroy a layered system [*Sleep*, 1988; *Davaille*, 1999a; *Gonnermann et al.*, 2002; *Jellinek and Manga*, 2002; *McNamara and Zhong*, 2004; *Zhong and Hager*, 2003]. However, none of our models has evolved into that stage, while reaching a steady state (Figure 5a). The horizontally averaged compositional field $C_{ave}(r)$ shows that the entrainment has not yet modified the two-layer structure significantly (Figure 5c).

[28] The three observables are determined in the same way as for isochemical models. For Case LMA1, T_{um} = 0.261, $T_p(r_{um})$ = 0.367 with standard deviation of 0.019, ΔT_{plume_um} = 0.41 with standard deviation of 0.07, and Q_{plume_um} = 17.5% with standard deviation of 2% (Table 2). Notice that plume temperature $T_p(r_{um})$ is significantly smaller than that from isochemical models, as indicated previously by *Farnetani* [1997]. However, because the upper mantle temperature T_{um} is also greatly reduced for thermochemical models, the normalized plume excess temperature ΔT_{plume_um} is not necessarily smaller than that for isochemical models.

[29] The internal heating rate for the whole mantle ζ_m is 65%. Internal heating rate for the top layer ζ_{top} is determined as 43% by using $\zeta_{top} = 1 - Q_{comp\_b}/Q_s$ where Q_{comp_b} is the heat flux across the compositional boundary and can be determined from total heat flux $Q(r)$ at the compositional boundary $r = r_{comp\_b} = r_{cmb} + d$ (Figure 5d). Notice that ζ_{top} should always be smaller than or equal to ζ_m, as the bottom layer may have nonzero internal heat generation. Also notice that plume heat flux Q_p(r) and downwelling heat flux Q_d(r) (Figure 5d for Q_p(r) and Q_d(r) in the top layer outside the TBLs) show similar dependences on r to those for isochemical models (Figure 2d). In summary for case LMA1 with ζ_{top} = 43%, plumes are too hot and transfer too much heat flux, and the upper mantle temperature is too cold, compared to the observed.

[30] Cases LMA2 and LMA3 are identical to Case LMA1 except that H_{top} is increased to 54 and 72, respectively. Mantle temperature increases with H_{top} in the top layer, but remains largely unchanged in the bottom layer (Figure 5c). Increasing H_{top} leads to larger ζ_m and ζ_{top}, but weaker plumes, and consequently smaller plume excess temperature ΔT_{plume_um} and plume heat flux Q_{plume_um} (Figure 5d and Table 2), similar to those in isochemical models. For Case LMA3, internal heating rate for the top layer ζ_{top} = 61%, internal heating rate for the whole mantle ζ_m = 78%, and three observables are: the upper mantle temperature T_{um} = 0.325, plume excess temperature ΔT_{plume_um} = 0.25, and plume heat flux Q_{plume_um} = 10.2%, all similar to the observed (Table 2). A resolution test for Case LMA3 in which the number of elements in horizontal directions is doubled shows the robustness of the results (Table 2).

[31] Six additional cases (Cases LMA4–9 in Table 2) are computed with Ra varying by a factor of 3, H_{top} varying between 18 and 72, H_{botm} varying between 54 and 108, and buoyancy number β varying between 2/3 and 3/2, but d_b is kept as 0.1. The three observables T_{um}, ΔT_{plume_um}, and Q_{plume_um} show similar dependences on ζ_{top} as in isochemical models; that is, as ζ_{top} increases, T_{um} increases, while ΔT_{plume_um} and Q_{plume_um} decrease (Figures 6a–6c). These three observations are well reproduced when ζ_{top} ~60–65% (Figures 6a–6c). The results are insensitive to Ra and β, although Ra is only varied by a factor of three (Table 2). Also notice that for a given internal heating rate for the top layer ζ_{top}, plume excess temperature ΔT_{plume_um} and upper mantle temperature T_{um} from thermochemical models are smaller than those from isochemical models with the same internal heating rate. This is similar to those in previous studies suggesting that the layered mantle models lead to smaller upper mantle temperature [*Spohn and Schubert*, 1982; *McNamara and van Keken*, 2000] and plume excess temperature [*Farnetani*, 1997].

[32] Four other cases (cases LMB1–4) are also computed with a thicker bottom layer or d_b = 0.176 (i.e., 1121 km). This increased d_b doubles the bottom layer volume compared with LMA models, and is similar to that of *Kellogg et al.* [1999]. Given that the results are rather insensitive to Ra and β as seen in isochemical models and LMA models, in these four cases, we only vary H_{top}, while $Ra = 1.2 \times 10^8$, β = 1, H_{botm} = 108 (Table 2). Similar dependences of upper mantle temperature T_{um}, plume excess temperature ΔT_{plume_um}, and plume heat flux Q_{plume_um} on internal heating rate for the top layer ζ_{top} are observed (Figures 6a–6c). When ζ_{top} ~60%, these three observations are reproduced.

[33] It is interesting to notice that for a given internal heating rate for the top layer ζ_{top}, T_{um} is greater for cases with larger d_b (Figure 6c). This is expected for spherical mantle convection in which $T_{um} \sim R^2_{comp\_b}/(R^2_e + R^2_{comp\_b})$ where R_{comp_b} is the average radius of the compositional boundary. Larger d_b leads to smaller curvature difference between the surface and compositional boundaries (i.e., R_e and R_{comp_b}), thus increasing the interior temperature. This increased T_{um} for cases with larger d_b is also responsible for the reduced ΔT_{plume_um} and Q_{plume_um} for these cases (Figures 6a–6c). Plume temperature $T_p(r_{um})$ for thermochemical models is weakly dependent on ζ_{top} and increases with ζ_{top} (Figure 6d). This arises because the temperature at the compositional boundary $T_{ave}(r_{comp\_b})$ (e.g., Figure 5c) shows similar dependence on ζ_{top} (Figure 6e), and because $T_{ave}(r_{comp\_b})$ controls the temperatures of the TBL and of plumes that are derived from the TBL. Plume temperature normalized by the temperature at the compositional bound-

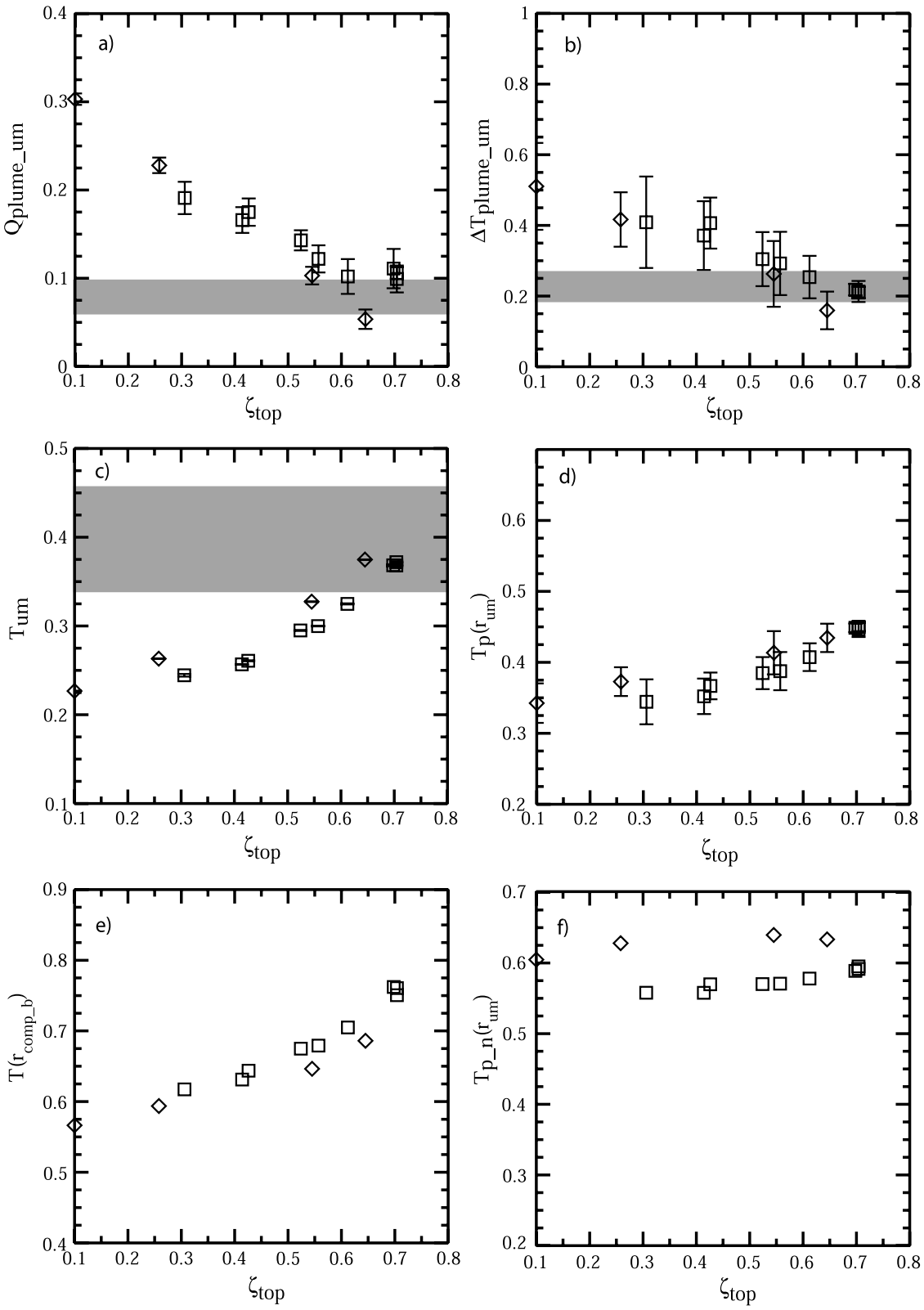

Figure 6. Dependences of (a) plume heat flux Q_{plume_um}, (b) plume excess temperature ΔT_{plume_um}, (c) upper mantle temperature T_{um}, (d) plume temperature $T_p(r_{um})$, (e) average temperature at the compositional boundary $T_{ave}(r_{comp\_b})$, and (f) normalized plume temperature by average temperature at the compositional boundary $T_{p\_n}(r_{um})$ on internal heating rate for the top layer ζ_{top} for thermochemical models (squares and diamonds for LMA and LMB cases, respectively). Standard deviations for Q_{plume_um}, ΔT_{plume_um}, and T_{um} and the range of observed values (shaded horizontal bars) are also plotted in Figures 6a–6c.

ary $T_{ave}(r_{comp\_b})$, $T_{p\_n}(r_{um})$, is nearly constant at ~0.6 (Figure 6f). However, $T_{p\_n}(r_{um})$ for LMB cases is generally larger than that for LMA cases, and they are all generally larger than $T_p(r_{um})$ for isochemical models (Figure 4d).

4. Discussions

[34] In this study, 3-D regional spherical models of mantle convection with relatively realistic mantle rheology and thermodynamic parameters are computed for different Rayleigh number, internal heating generation, buoyancy number and bottom layer thickness for layered mantle models. Plume excess temperature, plume heat flux, and mantle background temperature at the upper mantle depth (300 km depth) are quantified from these models and are compared with the observations. It was found that the controlling parameter for these three observables is the mantle internal heating rate for whole mantle convection (i.e., isochemical) or the internal heating rate for the top layer of a layered mantle (i.e., thermochemical). In order to reproduce the observed plume excess temperature, plume heat flux and the upper mantle temperature, internal heating rate for whole mantle convection needs ~65%, while for layered mantle, the internal heating rate for the top layer is 60–65% for the two bottom layer thicknesses considered. These results have implications for plume dynamics, the Earth's heat budget, CMB heat flux, layered mantle models and geochemistry.

4.1. Plume Dynamics

[35] Mantle plumes as a probe to mantle dynamics have been studied extensively since the plume idea was proposed by Morgan in 1970s. Two main geophysical observations associated with plumes are plume heat flux and plume excess temperature, both of which are constrained by surface observations, as reviewed recently by *Davies* [2005]. However, the estimate of plume heat flux has been debated. First, it was suggested that not all the hot spots used by *Davies* [1988] and *Sleep* [1990] in estimating plume heat flux are caused by mantle plumes [*Courtillot et al.*, 2003]. Second, it was suggested that not all the deep mantle plumes produce observable surface features. For the latter, it was proposed that there are as many as 5000 plumes in the mantle, but the majority of them, while together transferring significant heat flux, are too weak to produce surface volcanisms [*Malamud and Turcotte*, 1999]. It was also suggested that mantle plumes when ascending to weak asthenosphere may be homogenized and dispersed, thus becoming undetectable at the Earth's surface [*Montelli et al.*, 2004].

[36] A recent study on the dynamics of mantle plume population in 3-D high Ra convection models [*Zhong*, 2005] demonstrates that plume spacing is limited by the depth of the mantle even at very high Ra and that tens of plumes are expected, thus directly refuting the proposal for thousands of mantle plumes [*Malamud and Turcotte*, 1999]. The current study shows that the weak asthenosphere actually localizes mantle plumes and plume heat flux (Figure 3), while maintaining the general trend of total plume heat flux with depth (Figure 2d). That the plumes are localized in the upper mantle is consistent with the suggestion that Hawaiian plume may only be ~70 km in radius to explain vertical motion history of Hawaiian islands and swell topography [e.g., *Zhong and Watts*, 2002]. A unique aspect of the current study is that the controls on plume heat flux and plume excess temperature are examined simultaneously in 3-D models of multiple plumes. The model results show that plume heat flux and plume excess temperature are inherently related to each other and are both controlled by internal heating rate of the mantle. In particular, it is found that model plume heat flux and excess temperature either both satisfy or both violate the observations (Figure 4), and that for plume excess temperature of ~300 K, plume heat flux is expected to accounts for 6–10% of surface heat flux. This suggests that the plume heat flux estimated by *Davies* [1988] and *Sleep* [1990] is reasonable.

[37] In addition, it was suggested by *Farnetani* [1997] that layered mantle models can reproduce plume excess temperature of ~300 K but whole mantle convection often overpredicts the plume excess temperature. The current study shows that plume excess temperature can be explained in either whole mantle or layered mantle models, provided that mantle internal heating rate is sufficiently high (Figures 4b and 6b). Internal heating rate controls the plume excess temperature mainly by affecting upper mantle background temperature, as plume temperature is rather uniform for different model parameters and only depends on temperature at the CMB for whole mantle convection or at the compositional boundary for layered mantle models (Figures 4d and 6f).

4.2. Plume Heat Flux, CMB Heat Flux, and Earth's Heat Budget

[38] It is generally agreed that among the total heat flux out of the Earth's surface, ~36 TW is released via mantle convection, while ~7 TW is from radiogenic heating within continental crust [*Davies*, 1999]. The 36 TW mantle heat flux should consist of mantle internal heating (i.e., heating derived from mantle radioactive elements and mantle secular cooling) and heat flux from the core (i.e., heat flux at the CMB, Q_{cmb}). Q_{cmb} was estimated to be 2.4–3.5 TW on the basis of plume heat flux estimates [*Davies*, 1988, 1999; *Sleep*, 1990], as discussed earlier. This has led *Davies* [1999] to conclude that the mantle is 90% internally heated. However, considerations of core processes led to much higher estimates of Q_{cmb} ranging from 4 to 9 TW [*Anderson*, 2002], and possibly as high as 12 TW [*Gubbins et al.*, 2004; *Nimmo et al.*, 2004], implying much lower internal heating rate for the mantle.

[39] One crucial question is to what extent the plume heat flux represents the CMB heat flux Q_{cmb}. For example, it was suggested that the plume heat flux is only a lower bound on Q_{cmb}, as a significant fraction of Q_{cmb} may be consumed to heat up the cold downwellings [*Labrosse*, 2002]. However, in the current study, it was demonstrated that mantle plumes actually transfer the majority (~81%) of Q_{cmb} when the plumes just take off from the bottom TBL for whole mantle convection model (Figure 2d). That is, cold downwellings only consume relatively small but not insignificant amount of Q_{cmb}. The difference between the current study and that of *Labrosse* [2002] may be caused by temperature-dependent rheology and spherical geometry that were not included by *Labrosse* [2002] but are important for plume dynamics. However, the current study also found that the

plume heat flux at the upper mantle depth is not representative for Q_{cmb}. This is caused by adiabatic and diffusive cooling of mantle plumes as they ascend and subadiabaticity of ~180 K in mantle geotherm that together may reduce plume heat flux by a factor of 3 from large depths in the lower mantle to the upper mantle (Figure 2d).

[40] For whole mantle convection, the current study suggests that mantle internal heating rate ζ_m is ~65% or the CMB heat flux Q_{cmb} should account for 35% of surface heat flux Q_s. This amounts to Q_{cmb} of 12.6 TW and mantle internal heating of 23.4 TW, for surface mantle heat flux Q_s of 36 TW. For layered mantle models, the current study suggests that internal heating rate for the top layer ζ_{top} is ~60%, or 40% of Q_s (i.e., 14.4 TW) should come from the bottom layer to the top layer. This 14.4 TW is an upper bound on Q_{cmb}, because the bottom layer of the mantle which may be more enriched in radioactive elements may provide significant fraction of 14.4 TW that enters the top layer.

[41] Alternatively, we may estimate mantle internal heat generation rate from mantle secular cooling rate and mantle composition models. From studies of Archean MORB-like rocks from greenstone belts and ophiolite suites, *Abbott et al.* [1994] reported a mantle secular cooling rate $\dot{T}_{\rm sec}$ of 50–70 K/Ga. *Nisbet and Fowler* [1983] estimated ~100 K/Ga mantle cooling rate based on studies of Archean komatiites [*Green*, 1975; *Nisbet et al.*, 1993]. However, *Grove and Parman* [2004] indicated that the cooling rate estimates from Archean komatiites could be much smaller because the komatiites may be produced from wet and subduction settings. Thermal evolution models often suggest a mantle secular cooling rate $\dot{T}_{\rm sec}$ of 70–80 K/Ga [*Davies*, 1999; *Schubert et al.*, 2001]. If we take $\dot{T}_{\rm sec}$ = 70–80 K/Ga, then the heat flux from mantle secular cooling is $M_m\,\dot{T}_{\rm sec}\,c_p$ ~9.0–10.3 TW, where M_m is the mass of the mantle. Radiogenic heating for present-day Earth from the standard geochemical model (i.e., bulk silicate Earth model or BSE) is ~20.5 TW [e.g., *Workman and Hart*, 2005]. This leads to ~13.5 TW radiogenic heating for the mantle after excluding 7 TW for the continental crust. Adding together mantle radiogenic heating and heat flux from the secular cooling gives total mantle internal heating of 22.5–23.8 TW, which is generally consistent with the required 23.4 TW internal heating from our isochemical models with ζ_m ~65%. However, for layered mantle models, radiogenic heat generation rates for the top and bottom layers may differ significantly. The current study using plume related observations only constrains the internal heating rate for the top layer (e.g., ζ_{top} ~60%), although it may be considered as a lower bound on the internal heating rate for the whole mantle.

4.3. Layered Mantle Models, the Depleted Mantle Reservoirs, and Geochemistry

[42] The current study shows that for whole mantle convection, the CMB heat flux Q_{cmb} is required to be ~12.6 TW, which either exceeds estimated Q_{cmb} or is on the high end of estimated Q_{cmb} from other methods [*Anderson*, 2002; *Nimmo et al.*, 2004]. However, a compositionally heterogeneous or layered mantle as suggested by recent seismic observations [e.g., *Masters et al.*, 2000; *Ni et al.*, 2002] may reduce Q_{cmb} [e.g., *Davaille*, 1999a; *Tackley*, 1998]. For a layered mantle, the required internal heating rate for the top layer ζ_{top} may help constrain the radiogenic heat generation rate (i.e., composition) and total mass for the top layer.

[43] For a layered mantle, $M_{top}(\gamma_{top} + \dot{T}_{\rm sec}c_p) = Q_s\zeta_{top}$ is the energy balance for the top layer with mass M_{top}, radiogenic heat generation rate γ_{top}, and secular cooling rate $\dot{T}_{\rm sec}$. Given the weak dependence of the required ζ_{top} on bottom layer thickness (Figure 6), we assume that ζ_{top} ~60% is applicable to layered models with relatively thin bottom layer. Taking $Q_s \sim 36$ TW and $\dot{T}_{\rm sec} \sim 80$ K/Ga, a lower bound estimate of γ_{top} may be made by assuming that the top layer occupies nearly the whole mantle or $M_{top} \approx M_m$. The lower bound estimate of γ_{top} is 2.82×10^{-12} W/kg, and this estimate would be larger for a smaller $\dot{T}_{\rm sec}$. However, this lower bound estimate of γ_{top} at 2.82×10^{-12} W/kg is significantly larger than 0.76×10^{-12} W/kg for depleted MORB source (DMM) [e.g., *Workman and Hart*, 2005]. On the other hand, if we assume that the top layer consists of the DMM with radiogenic heat generation rate 0.76×10^{-12} W/kg and $M_{top} \approx M_m$, the mantle secular cooling rate $\dot{T}_{\rm sec}$ must be ~145 K/Ga to provide the required internal heating of 21.6 TW (i.e., 60%Q_s), and even larger $\dot{T}_{\rm sec}$ is needed for a smaller fraction of the mantle that the DMM occupies (i.e., $M_{top} < M_m$). This suggests that unless the mantle secular cooling rate $\dot{T}_{\rm sec}$ is greater than 145 K/Ga, the top layer cannot be the DMM at least in terms of radiogenic element concentration.

[44] If we assume that radiogenic heating elements of the mantle from the BSE model are uniformly distributed in the mantle, then average mantle radiogenic heat generation rate γ_{BSE_m} is ~3.33×10^{-12} W/kg (note that the radiogenic heat generation rate for the primitive mantle γ_{prim_m} is ~5.06×10^{-12} W/kg [e.g., *Workman and Hart*, 2005]). Taking ζ_{top} ~60%, Q_s ~36 TW and $\dot{T}_{\rm sec}$ ~80 K/Ga, and assuming that γ_{BSE_m} is an upper bound on radiogenic heat generation rate for the top layer γ_{top}, energy balance $M_{top}(\gamma_{top} + \dot{T}_{\rm sec}c_p) = Q_s\zeta_{top}$, leads to a lower bound estimate on the top layer mass M_{top} or the thickness of the top layer if the PREM density model is used. Such a lower bound estimate on the thickness of the top layer is 2520 km (i.e., an upper bound on the bottom layer thickness d_b at 350 km). A thinner top layer or thicker bottom layer is only possible if the secular cooling rate is significantly higher than 80 K/Ga or radiogenic heat generation rate for the top layer is higher than 3.33×10^{-12} W/kg.

[45] The above analyses suggest a layered mantle in which the top layer is relatively thick (>2520 km) with radiogenic heat generation rate $>2.82 \times 10^{-12}$ W/kg that is significantly larger than that for the DMM. The large layering depth is consistent with geodynamic studies on the spectra of thermochemical convection models and seismic structure [*Tackley*, 2002] and on the formation of the African and Pacific thermochemical anomalies in the lower mantle [*McNamara and Zhong*, 2005]. It is also supported by seismic studies on the large-scale structure of the mantle above the CMB [*Masters et al.*, 2000] and on mantle plumes that some of the plumes are originated at the CMB [*Montelli et al.*, 2004].

[46] The suggestion that the top layer of a layered mantle is significantly more enriched than the DMM is inconsistent

with conventional geochemical models for the MORBs [e.g., *Hofmann*, 1997; *Workman and Hart*, 2005]. However, the averaged MORB source composition depends on the choice of sampled ridge segments [*Su*, 2003]. More importantly, recent studies suggest that the melting, mixing and sampling processes in the shallow mantle should play an important role in affecting geochemical signatures of volcanic rocks including MORB and OIB [*Helffrich and Wood*, 1997; *Meibom and Anderson*, 2004; *Ito and Mahoney*, 2005]. For example, *Ito and Mahoney* [2005] show that the MORB and OIB may be derived from the same mantle source with radiogenic heat generation rate ranging from 1.52×10^{-12} to 3.04×10^{-12} W/kg (i.e., 30–60% of the primitive mantle heat generation rate). This is consistent with the required 2.82×10^{-12} W/kg or larger radiogenic heat generation rate for the top layer of the mantel from our models.

5. Conclusions

[47] Three-dimensional regional spherical models of mantle convection with extended-Boussinesq approximation and with depth- and temperature-dependent mantle viscosity and depth-dependent thermodynamic parameters are computed for different Rayleigh number, internal heat generation rate, buoyancy number, and bottom layer thickness for layered mantle models. Plume excess temperature, plume heat flux, and mantle background temperature at the upper mantle depth (300 km depth) are quantified from these models and are compared with the estimated values for the upper mantle to constrain thermochemical convection of the mantle. The main results can be summarized as follows.

[48] 1. The controlling parameter for observables: plume excess temperature, plume heat flux, and upper mantle temperature, is the internal heating rate for the mantle for whole mantle convection or the internal heating rate for the top layer of a layered mantle.

[49] 2. In order to reproduce the observed/estimated plume excess temperature, plume heat flux and the upper mantle temperature, internal heating rate for whole mantle convection needs ~65%, while for layered mantle, the internal heating rate for the top layer is 60–65% for bottom layer thicknesses <~1100 km.

[50] 3. The core heat flux is ~12.6 TW for whole mantle convection model, and this relatively large core heat flux implies that the mantle may be layered. For a layered mantle, an upper bound on the core heat flux is determined at ~14.4 TW, although the actual core heat flux may be much lower.

[51] 4. Immediately above the thermal boundary layer from which plumes are derived, plume heat flux accounts for the majority (~80%) of the heat flux across the boundary layer, confirming the original hypothesis by *Davies* [1988] and *Sleep* [1990] that core heat flux is largely released via mantle plumes in whole mantle convection. However, plume heat flux decreases significantly (i.e., by as much as a factor of 3) as plumes ascend through the mantle to the upper mantle, owing to the adiabatic and possibly diffusive cooling of the plumes and owing to a slight (~180 K) subadiabaticity in mantle geotherm, indicating that plume heat flux at the upper mantle depth inferred from surface swell topography and plate motion is not a good indicator of core heat flux.

[52] 5. Plume temperature in the upper mantle is ~0.5 of temperature at the CMB for whole mantle convection, independent of model parameters including internal heating rate and Rayleigh number. This suggests a CMB temperature of 3240°C, for plume temperature of 1620°C or plume excess temperature of 300°C in the upper mantle. For layered mantle models, the plume temperature is ~0.6 of temperature at the compositional interface, implying ~2700°C temperature at the interface and potentially significantly higher CMB temperature.

[53] 6. The top layer of a layered mantle is relatively thick (>2520 km) with radiogenic heat generation rate $>2.82 \times 10^{-12}$ W/kg which is more than 3 times of that for the depleted mantle source for the MORBs, for mantle secular cooling rate of 80 K/Ga. A thinner top layer with smaller radiogenic heat generation rate is possible only with larger secular cooling rate.

[54] Future studies are needed to examine the effects of larger viscosity variations associated with mantle plumes (i.e., larger activation energy) that may increase the vertical flow velocity of mantle plumes and hence plume heat transfer. Although the current study found no significant effects of buoyancy numbers, further studies with even smaller buoyancy number may be needed. Reduced buoyancy number may localize the dense components and expose the CMB directly to cold downwellings, which may resemble more present-day Earth's mantle [*Masters et al.*, 2000; *Ni et al.*, 2002, 2005; *Wen et al.*, 2001; *Wang and Wen*, 2004; *McNamara and Zhong*, 2005]. The larger viscosity contrasts and reduced buoyancy numbers may present significant computational challenges to currently available numerical models.

Appendix A: Numerical Methods and Benchmarks for Convection Code CitcomCU

[55] We first discuss numerical methods in CitcomCU and then present benchmark cases. The numerical methods for Cartesian CitcomCU are similar to those in the original Citcom [*Moresi and Gurnis*, 1996], except for new extensions including parallel computing, full multigrid solver [*Zhong et al.*, 2000], and particle-based advection scheme for thermochemical convection. The mathematical and numerical treatment of spherical geometry in CitcomCU is same as that in global spherical shell convection code CitcomS except for grid structure [*Zhong et al.*, 2000]. Regional spherical geometry in CitcomCU enables higher spatial resolution which is important for the current study on plume dynamics. *Billen et al.* [2003] published the first regional spherical models on subduction dynamics using an independent code.

[56] To model thermochemical convection, a particle ratio method [*Tackley and King*, 2003] is used in CitcomCU, similar to what has been recently done in CitcomS [*McNamara and Zhong*, 2004]. Because regional spherical models use regular grids with uniform spacings in colatitude θ and longitude ϕ directions, the implementation of the particle method is relatively straightforward, compared with that for global spherical models [*McNamara and Zhong*, 2004]. The particle-based advection scheme is similar to

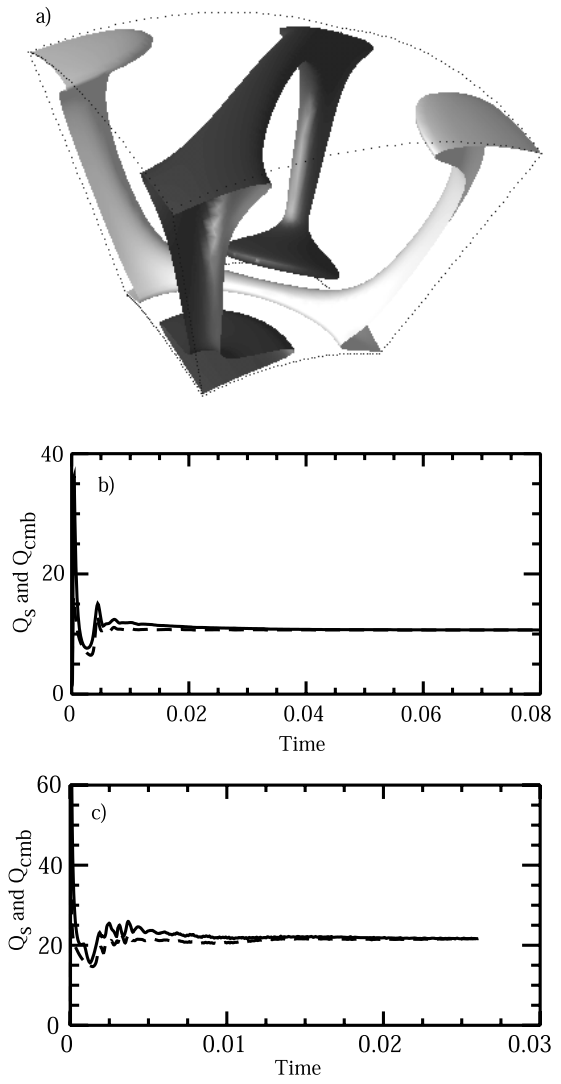

Figure A1. (a) Steady state thermal structure for Case A3, and time-dependent surface (solid line) and CMB (dashed line) heat fluxes for Cases (b) A3 and (c) A4.

that used by *Zhong and Hager* [2003] and *McNamara and Zhong* [2004]. The main features can be summarized as follows. For advection of compositional field C at a given time step, an Euler method is first used as a predictor to predict particle positions using velocity field from previous time step, V_o. The particle distribution is converted to compositional field C, using Tackley and King's particle-ratio method. This predicted C field coupled with thermal buoyancy is then used to determine a new velocity field, V_n. V_o and V_n are then used to determine the final particle positions for the current time step, using a second order Runge-Kutta scheme.

[57] Benchmark calculations using CitcomCU were done for isochemical and thermochemical convection in 3D Cartesian and regional spherical geometries. All the benchmark cases presented here assume an isoviscous flow, entirely basal heating, and the Boussinesq approximation. Isothermal and free-slip boundary conditions are applied at the top and bottom boundaries, while the sidewalls use thermally insulating and free-slip boundary conditions. In the benchmark calculations, isochemical convection models for different Rayleigh number are computed first to a steady state or statistically steady state, and the steady state temperature is then used as initial condition for thermochemical convection calculations. Entrainment in two-layer thermochemical convection continuously mixes the two layers and causes gradual reduction in the density difference between the two layers. This process may eventually homogenize the two fluids into a single layer fluid [*Davaille*, 1999a; *McNamara and Zhong*, 2004]. This benchmark study focuses on quantifying statistically steady state solutions before the two-layer fluid is completely homogenized.

[58] We first present calculations in regional spherical geometry. Isochemical convection calculations in regional spherical geometry are computed in a domain with inner radius $r_i = 0.55$ and outer radius $r_o = 1.0$, longitudes from $\phi_s = 0$ to $\phi_e = 36°$, and co-latitudes from $\theta_s = 73.5°$ to $\theta_e = 106.5°$ (i.e., centered at the equator) that has similar dimensions in each direction. The initial temperature is the

Table A1. Numerical Benchmarks From CitcomCU

Case	Ra	β	N_{ele}	N_{pe}	Q_s[a]	Q_{cmb}	V_s	V_{cmb}	ε_v, %	$\dot{C}_e$, %	$t_s - t_e$
A1	7×10^3	0	48^3	0	4.11	4.11	45.2	45.6			0.2–0.26
A2	10^4	0	48^3	0	4.75	4.75	59.8	60.4			0.23–0.33
A3	10^5	0	48^3	0	10.7	10.7	286.3	309.4			0.068–0.088
A4	10^6	0	64^3	0	21.7(0.0)[b]	21.6(0.1)	1178.6(4)	1393.4(6)			0.022–0.026
A5a	10^5	1	48^3	15	4.16(0.10)	4.14(0.06)	116.2(2)	151.3(2)	2.3	2.4(3.1)	0.035–0.055
A5b	10^5	1	48^3	30	4.21(0.03)	4.20(0.04)	120.4(2)	155.1(3)	2.0	2.0(2.2)	0.035–0.055
A5c	10^5	1	64^3	15	4.22(0.04)	4.22(0.04)	118.0(2)	154.8(1)	1.4	2.0(1.3)	0.035–0.055
A6a	10^6	1	64^3	15	8.96(0.3)	8.84(0.2)	559.7(15)	817.0(21)	0.7	7.4(9.4)	0.0125–0.0175
A6b	10^6	1	64^3	30	8.94(0.2)	8.92(0.1)	552.0(14)	809.7(16)	0.5	8.1(8.8)	0.0125–0.0175
A6c	10^6	1	96^3	15	9.07(0.2)	9.08(0.2)	563.4(12)	829.3(10)	0.3	5.3(8.4)	0.0125–0.0175
A7a	10^5	1	48^3	15	3.72(0.04)	3.69(0.03)	77.8(1.2)	51.2(1.0)	0.01	3.1(7.5)	0.15–0.25
A7b	10^5	1	48^3	30	3.72(0.04)	3.68(0.03)	77.5(1.2)	51.3(1.1)	0.04	3.6(6.5)	0.15–0.25
A7c	10^5	1	64^3	15	3.73(0.03)	3.71(0.02)	77.5(1.1)	51.3(0.7)	0.01	2.8(3.7)	0.15–0.25
A8a	10^6	1	64^3	15	7.38(0.5)	7.56(0.3)	335(27)	233(14)	0.09	20(37)	0.06–0.148
A8b	10^6	1	64^3	30	7.55(0.6)	7.69(0.3)	307(14)	212(11)	0.2	20(33)	0.06–0.148
A8c	10^6	1	96^3	15	7.77(0.5)	7.79(0.2)	324(19)	253(12)	0.03	16(28)	0.06–0.148

[a] N_{pe} is the number of particles per element. Q_s, Q_{cmb}, V_s, V_{cmb}, ε_v, $\dot{C}_e$, and $t_s - t_e$ are averaged surface heat flux, CMB heat flux, surface RMS velocity, CMB RMS velocity, relative error in total volume of dense component or $(C_t - C_{t\_0})/C_{t\_0}$ with C_{t_0} as the initial volume of dense component, entrainment rate, and starting and ending times over which the averages are computed.

[b] The numbers in parentheses are standard deviations. Note that Cases A1–A3 are in steady states with negligibly small standard deviations.

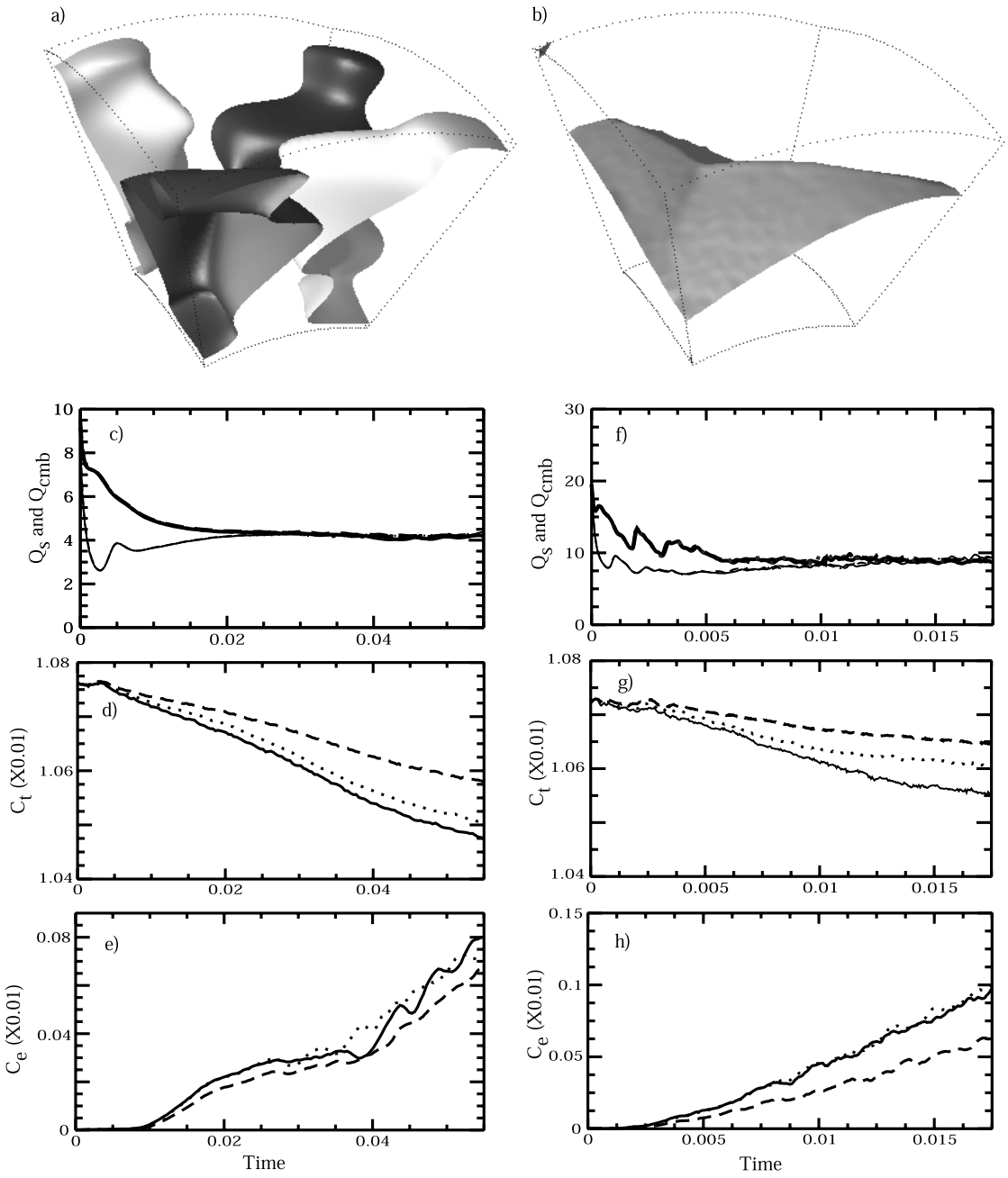

Figure A2. (a) Thermal and (b) compositional structures for Case A5a at t = 0.07155, (c) time dependence of surface (thin lines) and CMB (thick lines) heat fluxes, (d) the total volume of dense component, C_t, and (e) the volume of dense component above radius of 0.875, C_e for Cases A5a–A5c. (f, g, h) Corresponding plots to Figures A2c, A2d, and A2e for Cases A6a–A6c. In Figures A2d, A2e, A2g, and A2h, the solid, dotted, and dashed lines are for Cases a, b, and c, respectively

conductive temperature profile superimposed with harmonic perturbations

$$T(r,\theta,\phi) = \frac{r_i}{1-r_i}\left(\frac{1}{r}-1\right) + \delta T \sin\left[\frac{(1-r)\pi}{1-r_i}\right] \cdot \cos\left[\frac{(\theta-\theta_s)\pi}{\theta_e-\theta_s}\right]\cos\left[\frac{(\phi-\phi_s)\pi}{\phi_e-\phi_s}\right], \quad \text{(A1)}$$

where $\delta T = 10^{-3}$.

[59] Four isochemical calculations (Cases A1–A4 in Table A1) are computed for Rayleigh numbers *Ra* ranging from 7×10^3 to 10^6 at different resolutions. Table A1 lists averaged steady state heat fluxes and RMS velocities at the surface and bottom boundaries and their standard deviations. Figures A1a and A1b show for Case A3 with $Ra = 10^5$ the steady state residual temperature, and time-dependent surface and bottom heat fluxes, respectively. This case and other two cases with smaller *Ra* (Cases A1 and A2)

all reach a steady state with negligibly small standard deviations. For case A4 with $Ra = 10^6$, however, thermal structure never reaches a steady state even after 70,000 time steps, although averaged heat flux and velocities are in a statistically steady state (Figure A1c). Surface and bottom heat fluxes are balanced at accuracy of 0.6% or better for all the cases. Bottom RMS velocity is always larger than surface velocity and the difference is larger for larger Ra (Table A1).

[60] For two cases with $Ra = 10^5$ and 10^6, thermochemical convection calculations are computed with buoyancy number $\beta = 1$ for different numerical resolution and particle density (Cases A5a–A5c and A6a–A6c in Table A1). The compositional boundary is initially flat and is at the middle mantle depth with $r_{comp} = 0.775$. For Case A5a with $Ra = 10^5$, 48^3 elements, and on average 15 particles per element, Figures A2a, A2b, and A2c show thermal and compositional structure after 10,000 time steps of calculation, and time dependent surface and bottom heat fluxes, respectively. Evidently, heat fluxes reach statistically steady state for this layered convection calculation (Figure A2c).

[61] We also quantified time dependence of total volume of the dense component C_t and entrained dense component in the upper layer C_e that are defined as

$$C_t = \int_{r=r_i}^{1} C dv \tag{A2}$$

$$C_e = \int_{r=r_{comp}+0.1}^{1} C dv, \tag{A3}$$

where the integrals are volume-integrals, and C_e measures the entrainment [*van Keken et al.*, 1997]. For Case A5a, C_e increases with time, indicating continuous entrainment of the dense material into the top layer by upwellings, while C_t decreases with time (Figures A2d and A2e), indicating the limited accuracy of our particle advection scheme in conserving the mass. The averaged entrainment rate dC_e/dt and relative errors in mass conservation for C_t are given in Table A1, along with averaged surface and bottom heat fluxes and velocities. Increasing the number of particles reduces the entrainment rate slightly, but results in more noticeable improvement in the mass conservation (i.e., smaller reduction in C_t). Increasing the number of elements improves the mass conservation more significantly, and also results in a larger reduction in entrainment rate (Figures A2d and A2e). This is consistent with the conclusion of *van Keken et al.* [1997] and *Tackley and King* [2003] that particle-based advection methods are generally not suited for studies of entrainment. However, boundary heat fluxes are relatively insensitive to numerical resolutions (Figure A2c and Table A1), indicating that the advection scheme is sufficiently accurate for calculating heat fluxes. The cases with $Ra = 10^6$ show similar trends (Cases A6a–A6c in Table A1 and Figures A2f–A2h).

[62] Isochemical and isoviscous convection calculations using CitcomCU in a $1 \times 1 \times 1$ Cartesian box with Ra ranging from 10^4 to 10^6 is given by *Zhong* [2005]. The initial temperature for the isochemical calculations is given by

$$T(x,z) = 1 - z + \delta T \sin(\pi z)\cos\left(\frac{\pi x}{L}\right)\cos\left(\frac{\pi y}{L}\right), \tag{A4}$$

where $\delta T = 10^{-3}$ and $L = 1$. For two cases with $Ra = 10^5$ and 10^6 (Cases A7a–A7c, and A8a–A8c in Table A1), thermochemical convection calculations are computed with buoyancy number $\beta = 1$ for different numerical resolution and particle density. These Cartesian thermochemical convection calculations include an initially flat dense layer that occupies the bottom 40% of the box. The general characteristics of these cases are similar to those of *Tackley and King* [2003]. Table A1 lists the heat fluxes and entrainment rate averaged over a certain time period when the heat flux reaches a statistically steady state.

[63] **Acknowledgments.** This research is supported by National Science Foundation and David and Lucile Packard Foundation. The author would like to thank H. Cizkova, G. F. Davies, and Associate Editor C. Matyska for their constructive reviews and G. Ito and J. Lassiter for stimulating discussions.

References

Abbott, D., L. Burgess, J. Longhi, and W. H. F. Smith (1994), An empirical thermal history of the Earth's upper mantle, *J. Geophys. Res.*, *99*, 13,835–13,850.

Anderson, O. L. (2002), The power balance at the core-mantle boundary, *Phys. Earth Planet. Inter.*, *131*, 1–17.

Billen, M. I., M. Gurnis, and M. Simons (2003), Multiscale dynamic models of the Tonga-Kermadec subduction zone, *Geophys. J. Int.*, *153*, 359–388.

Boehler, R., A. Chopelas, and A. Zerr (1995), Temperature and chemistry of the core-mantle boundary, *Chem. Geol.*, *120*, 199–205.

Christensen, U. R., and D. A. Yuen (1985), Layered convection induced by phase changes, *J. Geophys. Res.*, *90*, 10,291–10,300.

Courtillot, V., A. Davaille, J. Besse, and J. Stock (2003), Three distinct types of hotspots in the Earth's mantle, *Earth Planet. Sci. Lett.*, *205*, 295–308.

Davaille, A. (1999a), Simultaneous generation of hotspots and superswells by convection in a heterogeneous planetary mantle, *Nature*, *402*, 756–760.

Davaille, A. (1999b), Two-layer thermal convection in miscible viscous fluids, *J. Fluid Mech.*, *379*, 223–253.

Davies, G. F. (1988), Ocean bathymetry and mantle convection: 1. Large-scale flow and hotspots, *J. Geophys. Res.*, *93*, 10,467–10,489.

Davies, G. F. (1999), *Dynamic Earth: Plates, Plumes and Mantle Convection*, 458 pp., Cambridge Univ. Press, New York.

Davies, G. F. (2005), A case for mantle plumes, *Chin. Sci. Bull.*, *50*, 1541–1554.

Farnetani, C. G. (1997), Excess temperature of mantle plumes: The role of chemical stratification across D″, *Geophys. Res. Lett.*, *24*, 1583–1586.

Gonnermann, H. M., M. Manga, and A. M. Jellinek (2002), Dynamics and longevity of an initially stratified mantle, *Geophys. Res. Lett.*, *29*(10), 1399, doi:10.1029/2002GL014851.

Green, D. H. (1975), Genesis of Archean peridotitic magmas and constraints on Archean geothermal gradients and tectonics, *Geology*, *3*, 15–18.

Grove, T. L., and S. W. Parman (2004), Thermal evolution of the Earth as recorded by komatiites, *Earth Planet. Sci. Lett.*, *219*, 173–187.

Gubbins, D., D. Alfe, G. Masters, D. Price, and M. Gillan (2004), Gross thermodynamics of 2-component core convection, *Geophys. J. Int.*, *157*, 1407–1414.

Hager, B. H., and M. A. Richards (1989), Long-wavelength variations in Earth's geoid: Physical models and dynamical implications, *Philos. Trans. R. Soc., Ser. A*, *328*, 309–327.

Helffrich, G. R., and B. J. Wood (1997), The Earth's mantle, *Nature*, *412*, 501–507.

Hofmann, A. W. (1997), Mantle geochemistry: The message from oceanic volcanism, *Nature*, *385*, 219–229.

Ishii, M., and J. Tromp (1999), Normal-mode and free-air gravity constraints on lateral variations in velocity and density of Earth's mantle, *Science*, *285*, 1231–1236.

Ito, G., and J. J. Mahoney (2005), Flow and melting of a heterogeneous mantle: 2. Implications for a chemically non-layered mantle, *Earth Planet. Sci. Lett.*, *230*, 47–63.

Jellinek, A. M., and M. Manga (2002), The influence of a chemical boundary layer on the fixity, spacing, and lifetime of mantle plumes, *Nature*, *418*, 760–763.

Kellogg, L. H., B. H. Hager, and R. van der Hilst (1999), Compositional stratification in the deep mantle, *Science*, *283*, 1881–1884.

Labrosse, S. (2002), Hotspots, mantle plumes and core heat loss, *Earth Planet. Sci. Lett.*, *199*, 147–156.

Malamud, B. D., and D. L. Turcotte (1999), How many plumes are there?, *Earth Planet. Sci. Lett.*, *174*, 113–124.

Masters, G., G. Laske, H. Bolton, and A. Dziewonski (2000), The relative behavior of shear velocity, bulk sound speed, and compressional velocity in the mantle: Implications for chemical and thermal structure, in *Earth's Deep Interior: Mineral Physics and Tomography From the Atomic to the Global Scale*, *Geophys. Monogr. Ser.*, vol. 117, edited by S. Karato et al., pp. 63–87, AGU, Washington, D. C.

McNamara, A. K., and P. E. van Keken (2000), Cooling of the Earth: A parameterized convection study of whole versus layered models, *Geochem. Geophys. Geosyst.*, *1*, doi:10.1029/2001GC000045.

McNamara, A. K., and S. Zhong (2004), Thermochemical structures within a spherical mantle: Superplumes or piles?, *J. Geophys. Res.*, *109*, B07402, doi:10.1029/2003JB002847.

McNamara, A. K., and S. Zhong (2005), Thermochemical piles under Africa and the Pacific, *Nature*, *437*, 1136–1139.

Meibom, A., and D. L. Anderson (2004), The statistical upper mantle assemblage, *Earth Planet. Sci. Lett.*, *217*, 123–139.

Montelli, R., G. Nolet, F. A. Dahlen, G. Masters, E. R. Engdahl, and S. H. Hung (2004), Finite frequency tomography reveals a variety of plumes in the mantle, *Science*, *303*, 338–343.

Moresi, L., and M. Gurnis (1996), Constraints on the lateral strength of slabs from three-dimensional dynamic flow models, *Earth Planet. Sci. Lett.*, *138*, 15–28.

Morgan, W. J. (1971), Convection plumes in the lower mantle, *Nature*, *230*, 42–43.

Ni, S. D., E. Tan, M. Gurnis, and D. Helmberger (2002), Sharp sides to the African superplume, *Science*, *296*, 1850–1852.

Ni, S. D., D. Helmberger, and J. Tromp (2005), Three-dimensional structure of the African superplume from waveform modeling, *Geophys. J. Int.*, *161*, 283–294.

Nimmo, F., G. D. Price, J. Brodholt, and D. Gubbins (2004), The influence of potassium on core and geodynamo evolution, *Geophys. J. Int.*, *156*, 363–376.

Nisbet, E. G., and C. M. R. Fowler (1983), Model for Archean plate tectonics, *Geology*, *11*, 376–379.

Nisbet, E. G., M. J. Cheadle, N. T. Arndt, and M. J. Bickle (1993), Constraining the potential temperature of the Archean mantle—A review of evidence from komatiites, *Lithos*, *30*, 291–307.

Roberts, J. H., and S. Zhong (2004), Plume-induced topography and geoid anomalies and their implications for the Tharsis Rise on Mars, *J. Geophys. Res.*, *109*, E03009, doi:10.1029/2003JE002226.

Schilling, J.-G. (1991), Fluxes and excess temperatures of mantle plumes inferred from their interaction with migrating midocean ridges, *Nature*, *352*, 397–403.

Schubert, G., D. L. Turcotte, and P. Olson (2001), *Mantle Convection in the Earth and Planets*, 940 pp., Cambridge Univ. Press, New York.

Sleep, N. H. (1988), Gradual entrainment of a chemical layer at the base of the mantle by overlying convection, *Geophys. J.*, *95*, 437–447.

Sleep, N. H. (1990), Hotspots and mantle plumes: Some phenomenology, *J. Geophys. Res.*, *95*, 6715–6736.

Spohn, T., and G. Schubert (1982), Modes of mantle convection and the removal of heat from the Earth's interior, *J. Geophys. Res.*, *87*, 4682–4696.

Su, W. J., and A. M. Dziewonski (1997), Simultaneous inversion for 3-D variations in shear and bulk velocity in the mantle, *Phys. Earth Planet. Inter.*, *100*, 135–156.

Su, Y. J. (2003), Global MORB chemistry compilation at segment scale, Ph.D. thesis, Dep. of Earth and Environ. Sci., Columbia Univ., New York.

Tackley, P. J. (1998), Three-dimensional simulations of mantle convection with a thermochemical CMB boundary layer: D″?, in *The Core-Mantle Boundary Region*, *Geodyn. Ser.*, vol. 28, edited by M. Gurnis et al., pp. 231–253, AGU, Washington, D. C.

Tackley, P. J. (2002), Strong heterogeneity caused by deep mantle layering, *Geochem. Geophys. Geosyst.*, *3*(4), 1024, doi:10.1029/2001GC000167.

Tackley, P. J., and S. D. King (2003), Testing the tracer ratio method for modeling active compositional fields in mantle convection simulations, *Geochem. Geophys. Geosyst.*, *4*(4), 8302, doi:10.1029/2001GC000214.

Turcotte, D. L., and G. Schubert (2002), *Geodynamics*, 2nd ed., Cambridge Univ. Press, New York.

van Keken, P. E., S. D. King, H. Schmeling, U. R. Christensen, D. Neumeister, and M.-P. Doin (1997), A comparison of methods for the modeling of thermochemical convection, *J. Geophys. Res.*, *102*, 22,477–22,496.

Wang, Y., and L. Wen (2004), Mapping the geometry and geographic distribution of a very-low velocity province at the base of the Earth's mantle, *J. Geophys. Res.*, *109*, B10305, doi:10.1029/2003JB002674.

Wen, L. X., P. Silver, D. James, and R. Kuehnel (2001), Seismic evidence for a thermo-chemical boundary layer at the base of the Earth's mantle, *Earth Planet. Sci. Lett.*, *189*, 141–153.

Wolfe, C. J., I. T. Bjarnason, J. C. Vandecar, and S. C. Soloman (1997), Seismic structure of the Iceland mantle plume, *Nature*, *385*, 245–247.

Workman, R. K., and S. R. Hart (2005), Major and trace element composition of the depleted MORM mantle (DMM), *Earth Planet. Sci. Lett.*, *231*, 53–72.

Zhong, S. (2005), Dynamics of thermal plumes in 3D isoviscous thermal convection, *Geophys. J. Int.*, *162*, 289–300.

Zhong, S., and B. H. Hager (2003), Entrainment of a dense layer by thermal plumes, *Geophys. J. Int.*, *154*, 666–676.

Zhong, S., and A. B. Watts (2002), Constraints on the dynamics of mantle plumes from uplift of Hawaiian islands, *Earth Planet. Sci. Lett.*, *203*, 105–116.

Zhong, S., M. T. Zuber, L. N. Moresi, and M. Gurnis (2000), Role of temperature dependent viscosity and surface plates in spherical shell models of mantle convection, *J. Geophys. Res.*, *105*, 11,063–11,082.

S. Zhong, Department of Physics, University of Colorado at Boulder, Boulder, CO 80309, USA. (szhong@anquetil.colorado.edu)